PHYSICAL REVIEW D **108,** 034030 (2023)

Precision studies of the post-CT18 LHC Drell-Yan data in the CTEQ-TEA global analysis

Ibrahim Sitiwaldi,[1,*] Keping Xie,[2,†] Alim Ablat,[1,‡] Sayipjamal Dulat,[1,§] Tie-Jiun Hou,[3,‖] and C.-P. Yuan[4,¶]

(CTEQ-TEA Collaboration)

[1]*School of Physics Science and Technology, Xinjiang University, Urumqi, Xinjiang 830046 China*
[2]*Pittsburgh Particle Physics, Astrophysics, and Cosmology Center, Department of Physics and Astronomy, University of Pittsburgh, Pittsburgh, Pennsylvania 15260, USA*
[3]*School of Nuclear Science and Technology, University of South China, Hengyang, Hunan 421001, China*
[4]*Department of Physics and Astronomy, Michigan State University, East Lansing, Michigan 48824, USA*

(Received 7 June 2023; accepted 31 July 2023; published 29 August 2023)

In this study, we examine closely the impact of the post-CT18 LHC Drell-Yan data on parton distribution functions (PDFs) in the general CTEQ-TEA global analysis framework. We compare the two main theoretical predictions, the MCFM fixed order calculations at next-to-next-to-leading order (NNLO) and the ResBos2 NNLO matched to q_T resummation up to next-to-next-to-next-to-leading logarithmic (N3LL) level. We find that the overall inclusive cross sections agree well but the fiducial distributions can differ at a percent level. We mainly discuss the result of the ResBos2 resummation calculation which yields a smaller Monte Carlo uncertainty, and a better description to the post-CT18 LHC Drell-Yan data. We find that the majority of post-CT18 LHC Drell-Yan data are consistent with the ATLAS 7 TeV W, Z data, which were included in the CT18A, but not CT18, fit and increases the strange-quark distribution at the small x region. The noticeable exception is that the ATLAS and LHCb 8 TeV W data pull $d(\bar{d})$ quark PDFs to the opposite direction with respect to the ATLAS 7 TeV W, Z data. The inclusion of these post-CT18 LHC Drell-Yan datasets in the CTEQ-TEA global analysis is to update the CT18 PDFs following similar trends as CT18Z PDFs. The parton luminosities and a few phenomenological implications with the fiducial $W^{\pm}, Z$ and inclusive $H, t\bar{t}, t\bar{t}H$ productions at the 14 TeV LHC, as examples, are presented.

DOI: 10.1103/PhysRevD.108.034030

I. OVERVIEW

The Drell-Yan mechanism, first introduced by Sidney Drell and Tung-Mow Yan [1], describes the lepton-pair production through quark-antiquark annihilation in hadron collisions. It turns out to be a cornerstone process to establish the strong interaction theory, i.e., quantum chromodynamics (QCD). The charged- and neutral-current Drell-Yan productions at the superproton synchrotron (SPS) led to the discoveries of the W [2,3] and Z [4,5] bosons, separately observed by UA1 and UA2 Collaborations. Meanwhile, the Drell-Yan production can also provide a precise determination of the Standard Model (SM) parameters, such as the weak-mixing angle [6–8], the strong coupling [9], and the weak-boson widths and branching ratios [10]. The latest high-precision measurement of W-boson mass performed by the CDF Collaboration based on the Tevatron Run II data shows a 7σ deviation from the SM expectation [11], which inspires numerous Beyond the Standard Model (BSM) explanations. In modern global QCD analyzes [12–18], the Drell-Yan production plays a crucial role in constraining the parton distribution functions (PDFs).

The accumulation of high-quality data at the Large Hadron Collider (LHC) brings the experimental uncertainties to a percent or subpercent precision level for many SM processes, especially for the Drell-Yan production. It mandatorily requires theoretical precision to enter the same level to analyze these data. Currently, next-to-next-to-leading order (NNLO) calculations in terms of the perturbative expansion of the strong coupling become a

---

[*] ibrahim010@sina.com
[†] xiekeping@pitt.edu
[‡] alimablat@stu.xju.edu.cn
[§] Corresponding author: sdulat@hotmail.com
[‖] tjhou@msu.edu
[¶] yuanch@msu.edu

state-of-the-art [19]. In some instances, even the next-to-NNLO (N3LO) accuracy for some processes (such as Drell-Yan and Higgs productions) becomes available, and for some processes is in progress [20]. Meanwhile, next-to-leading order (NLO) corrections in terms of quantum electrodynamics (QED) (or electroweak in a more general sense) are also necessary for some specific processes [21–23].

Specifically for the Drell-Yan production, the NNLO fixed-order correction to the total cross section has been known for three decades [24]. The NNLO dilepton rapidity distribution of the virtual photon produced in the Drell-Yan process came afterwards [25,26], followed by the fully differential kinematics in the leptonic decay of the vector boson $(W, Z/\gamma^*)$, including the γ-Z interference, finite-width effects, as well as spin correlations [27–29]. Nowadays, a few public NNLO codes with different subtraction schemes are available, such as the transverse moment (q_T) subtraction in DYNNLO [29,30] and MATRIX [31], the sector decomposition in FEWZ [32,33], and the N-jettiness in MCFM [34,35]. On the other side, the q_T resummation calculation for Drell-Yan vector boson production has been established even for a longer time firstly with the Collins-Soper-Sterman (CSS) formalism [36], and later reorganized by Catani, Cieri, de Florian, and Grazzini [37]. Recently, the soft-collinear effective theory (SCET) [38–42] provides a convenient framework to perform the resummation up to higher orders [43–45]. Based on various techniques, the predictions of q_T resummation calculation also became available in a few public codes, such as ResBos(2) [46–48], DYRes [49], DYqT [50,51], DYTurbo [52], and CuTe [44,53].

Recently, based on the antenna subtraction method, the Drell-Yan inclusive cross section was calculated up to N3LO [54,55]. Afterwards, based on the q_T subtraction method, the Drell-Yan N3LO cross sections have been calculated either inclusively [56], or fully exclusively, with the q_T resummation matched to the next-to-next-to-next-to-leading logarithimic (N3LL) level [57,58] and beyond [59]. In the meantime, the next-to-leading order electroweak (EW) corrections have been known in Refs. [60,61]. Very recently, the mixed QCD-EW corrections have also been computed for the neutral-current Drell-Yan dilepton production at hadron colliders, which are found to be within a percent level for the invariant mass and (potentially) rapidity distributions [62].

In this work, we will follow the QCD global analysis presented in Refs. [14,63] and mainly consider the NNLO QCD fixed order calculation with the MCFM [35] as well as the matched q_T resummation calculation up to N3LL, provided by the ResBos2 program [48]. A minor difference up to a percent level is found in these two calculations. A similar level of difference also shows up with different NNLO subtraction methods. See Appendix F of Ref. [14] or Ref. [64] for details.

The Drell-Yan production has been precisely measured at the LHC, mostly delivered by ATLAS, CMS, and LHCb Collaborations. Many Run I and Run II data have already been closely inspected and partially included in the global analysis of parton distribution functions (PDFs) of proton performed by various groups [13–18]. In comparison with the proton-antiproton colliders, such as SPS or Tevatron, the LHC as a proton-proton collider embraces an advantage to provide more insights into the proton's light sea-quark decomposition, as a result of that one initial parton in the quark-antiquark annihilation must come from the sea quarks. As mentioned, with the reduction of experimental uncertainties, especially the statistical ones, a consistent theoretical description of data becomes more and more of a challenge. In many scenarios, the theoretical uncertainties, especially the PDF uncertainty, become a bottleneck for precision theoretical predictions or Monte Carlo simulations [11,65]. All these aspects motivate the present study to understand the impact of the LHC precision Drell-Yan data on the CTEQ-TEA global QCD analysis of proton PDFs.

This paper is organized as follows. In Sec. II, we will summarize the measurements of Drell-Yan production made by the ATLAS, CMS, and LHCb experiments at the LHC and emphasize those in the post-CT18 era. Meanwhile, we will describe the theoretical predictions for these data, with the comparison of the MCFM NNLO fixed-order calculation and the ResBos2 NNLO + N3LL resummation calculation (denoted as "N3LL" in the rest of this work). The correlation between the data and the PDFs will be presented as well. In Sec. III, we will examine the individual impact of these new Drell-Yan data on the three ensembles (CT18, CT18A [14], and CT18As [66]) of PDFs, both using the ePump's fast Hessian profiling technique [67,68], and the CTEQ-TEA global analysis. The simultaneous fits of these post-CT18 DY data together with the corresponding phenomenological implications are presented in Sec. IV. In Sec. V, we will provide our conclusion and discussion. For completeness, some additional figures are collected in Appendix.

II. POST-CT18 LHC DRELL-YAN DATA

Since the CT14 era [63], the CTEQ-TEA global analysis began to include the LHC Run I data, with matrix elements calculated with the CTEQ internal codes and K-factors extracted from the ResBos [46,47], FEWZ [32,33], or VRAP [25,26]. Specifically for Drell-Yan datasets, CT14 includes the LHCb 7 TeV inclusive W/Z production [69], CMS 7 TeV muon [70] and electron [71] charge asymmetry in W-boson decays, and the ATLAS 7 TeV Drell-Yan ($W^\pm$ and Z/γ^*) production [72]. These CMS and ATLAS 7 TeV datasets were inherited in the CT18 analysis [14], while the LHCb one is updated with a higher-luminosity data [73]. Meanwhile, more LHC Run I Drell-Yan data were included in the CT18 analysis, with the fast interpolation grid technique, APPLgrid [74], generated with MCFM-6.8 [75] and aMCfast [76], together with NNLO K-factors generated with MCFM-8 [34,77] and FEWZ [32,33].

After the release of the CT18 PDFs, more Drell-Yan data become available. We summarize the ones relevant to this study as follows:

(i) *ATL5WZ*. The ATLAS Collaboration measured $W^\pm$- and Z-boson productions in pp collisions at the $\sqrt{s} = 5.02$ TeV, which serve as an important reference for $W^\pm$ and Z-boson productions in proton-lead (p + Pb) and lead-lead (Pb + Pb) collisions at the same center-of-mass energy. The inclusive $W^\pm$- and Z-boson productions were measured for the fiducial integrated and differential cross sections with an integrated luminosity of 25 pb^{-1} [78], which we will dub as ATL5WZ as follows. The fiducial phase space is defined as

$$p_T^{\ell,\nu} > 25\,\text{GeV}, \quad |\eta_\ell| < 2.5, \quad m_T > 40\,\text{GeV}, \tag{1}$$

for $W^\pm$ production, and

$$p_T^{\ell} > 20\,\text{GeV}, \quad |\eta_\ell| < 2.5, \quad 66 < m_{\ell\ell} < 116\,\text{GeV}, \tag{2}$$

for on shell Z production. The transverse mass of lepton-neutrino system is defined as $m_T = \sqrt{2 p_T^\ell p_T^\nu (1 - \cos\Delta\phi)}$, where $\Delta\phi$ is the azimuthal angle between $\vec{p}_T^{\,\ell}$ and $\vec{p}_T^{\,\nu}$.

In the upper panels of Fig. 1, we present the theoretical predictions obtained with CT18 NNLO PDFs by using the MCFM-6.8 NLO [75], MCFM-8 NNLO [34,77], and ResBos NLO fixed order [46,47] as well as ResBos2 q_T resummation up to the N3LL + NNLO (denoted as "N3LL") level [48] calculations. Throughout this work, the renormalization and factorization scales (μ_R and μ_F) are set to the invariant mass of the vector boson m_Z or m_W. We use MCFM-6.8 to generate the fast computational APPLgrid [74] tables. We have checked that both the MCFM-8 and ResBos NLO fixed order calculations reproduce the MCFM-6.8 results at the NLO, as shown in Fig. 1. The K-factors were calculated as ratios to the MCFM-6.8 prediction, as shown in the lower insets of upper panels of Fig. 1. We see that the differential fiducial cross section of Drell-Yan production predicted by the MCFM NNLO fixed-order calculation can differ from the ResBos2 resummation prediction by a percent level. Recall that different NNLO codes, such as FEWZ, DYNNLO, and MCFM (with different subtraction schemes), can yield different predictions, at the percent level, on the differential fiducial cross section of Drell-Yan production, though their predictions agree well in total inclusive cross section [14,64]. This is because when both leptons of the Drell-Yan pair are required to have the same minimum values of transverse momentum, the transverse momentum of the Drell-Yan pair is about zero. In that kinematic region, a resummation calculation, summing up the effect of multiple soft-gluon emissions, can provide better prediction than a fixed-order calculation (which

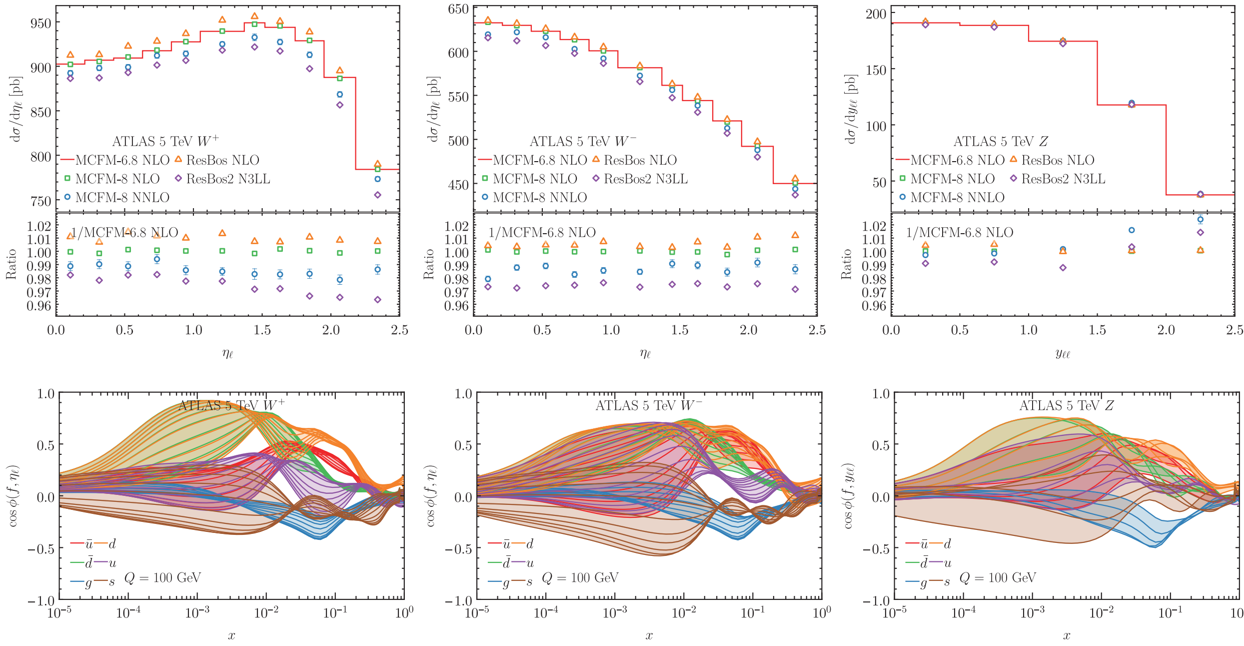

FIG. 1. The comparison of CT18 predictions for the ATLAS 5.02 TeV W/Z data (upper panels), and the correlation cosines between the CT18 PDFs and the ATLAS 5.02 TeV W/Z data points (lower panels).

yields a singular result as the transverse momentum of the Drell-Yan pair approaches to zero). Hence, in this work, we will focus on the ResBos predictions, unless specified otherwise. In general, we found that the Monte Carlo uncertainty of the MCFM NNLO predictions is larger than that of ResBos2, which in principle can be improved by increasing the statistics. However, with a limited resource of computation power, we get a better convergence in the Resbos2 N3LL calculation. Comparing global fits with these two types of K-factors, we normally found a better χ^2 for the ResBos N3LL predictions. For this reason, we will mainly present the fitted results with the ResBos K-factors in this work.

A similar comparison between the experimental data and theoretical predictions, after including the post-CT18 LHC Drell-Yan data in a global fit, will be presented in Sec. IV.

In the lower panels of Fig. 1, we show the correlation cosine [79] between the ATLAS 5.02 TeV W/Z boson production data and the CT18 PDFs at $Q = 100$ GeV. We see that the ATLAS 5.02 TeV W^+ data gives a large correlation to the $\bar{d}(d)$ PDFs around $x \sim 10^{-3}$. It can be understood in terms of the LO partonic process $u\bar{d} \to W^+$, which directly probes the $\bar{d}$ PDF. The large d quark PDF correlation originates from the co-evolution of d and $\bar{d}$ PDFs due to the $g \to d\bar{d}$ splitting. In comparison, the $\bar{u}d \to W^-$ production gives large correlation to the $\bar{u}(u)$ PDFs, with a slightly milder value than the $\cos\phi(d(\bar{d}), W^+)$. It can be understood that the valence u quark PDF is better constrained than d quark PDF with the deep-inelastic scattering (DIS) data. For this reason, the ATLAS 5.02 TeV W^- data can also constrain the d quark PDF. Finally, the ATLAS 5.02 TeV Z production data gives a large correlation to $d(\bar{d})$ PDFs and a slightly smaller correlation to $u(\bar{u})$.

(ii) *ATL8W*. The W production in the muonic decay channel $(W \to \mu\nu)$ at the LHC 8 TeV was measured by the ATLAS Collaboration with the 20.2 fb^{-1} integrated luminosity [80]. We will call it ATL8W in this work. The fiducial volume is defined as in Eq. (1), except the absolute muon pseudorapidity is required as $|\eta_\ell| < 2.4$. The data were released in terms of the differential cross section as well as the charge asymmetry with respect to the muon pseudorapidity. Similarly, in Fig. 2, we compare the CT18 theoretical predictions in the upper panels and the corresponding correlation cosine in the lower panels. The main features of correlation already show up in the ATLAS 5.02 TeV case, while the specific strongly correlated x value becomes slightly smaller due to the larger collision energy, in terms of the $x \sim (M_W/\sqrt{s})e^{\pm y}$ dependence. As we will see later, the ATL8W data can provide a strong constraint on $d(\bar{d})$-quark PDFs around $x \sim 10^{-3}$.

(iii) *ATL8Z3D*. The neutral-current Drell-Yan production at the LHC 8 TeV for both electron and muon decay channels was measured by the ATLAS Collaboration with an integrated luminosity of 20.2 fb^{-1} [81]. For the central leptons, the fiducial region is defined as

$$p_T^\ell > 20\,\text{GeV}, \quad |\eta_\ell| < 2.4, \quad 46 < m_{\ell\ell} < 200\,\text{GeV}. \tag{3}$$

The data were presented as a triple differential distribution in terms of invariant mass $m_{\ell\ell}$, rapidity of dilepton $y_{\ell\ell}$, and cosine of the Collin-Soper angle $\cos\theta^*$,[1] which we name as ATL8Z3D. Similar to the ATLASpdf21 [18] analysis, we do not consider the high-rapidity electron channel in this work.

For this dataset, we obtain the theoretical predictions directly from the ATLAS Collaboration, which was employed in the ATLASpdf21 PDF determination [18] with the xFitter framework [83]. In this analysis, the NLO predictions are calculated by using APPLgrid [74], generated with the MCFM-6.8 [75], while NNLO QCD and NLO EW corrections are folded into the K-factors with NNLOJET [84]. Meanwhile, the K-factors provided by the ATLAS Collaboration also incorporate the acceptance of the lepton fiducial cuts for every $(m_{\ell\ell}, y_{\ell\ell}, \cos\theta^*)$ bin. The theoretical predictions in comparison with data before and after including this dataset in global fits will be presented later. We remind readers that the MSHT20 and NNPDF4.0 treated this data differently from ATLASpdf21 and this study. Namely, in their PDF analyses, they have summed over the $\cos\theta^*$ bins to obtain the double differential distributions in terms of $(m_{\ell\ell}, y_{\ell\ell})$, which correspond to a smaller number of data points.

In Fig. 3, we show the correlation cosine of the ATLAS 8 TeV Z 3D data and the CT18 PDFs. Similar to ATLAS 5.02 TeV Z case, we obtain somewhat larger correlation to the $u(\bar{u})$, $d(\bar{d})$ and $s(\bar{s})$[2] PDFs. This can be understood that this triple differential distribution can provide more exclusive information to constrain the PDFs in terms of the (x, Q) kinematics.

---

[1] The cosine of the Collins-Soper angle is defined as $\cos\theta^* = \frac{p_{z,\ell\ell}}{m_{\ell\ell}|p_{z,\ell\ell}|}\frac{p_1^+ p_2^- - p_1^- p_2^+}{\sqrt{m_{\ell\ell}^2 + p_{T,\ell\ell}^2}}$, where $p_i^\pm = E_i \pm p_{z,i}$ and $i = 1, 2$ denote the negatively and positive charged leptons [82].

[2] The CT18 fit assumes $s = \bar{s}$ at the starting scale $Q_0 (= 1.3$ GeV$)$.

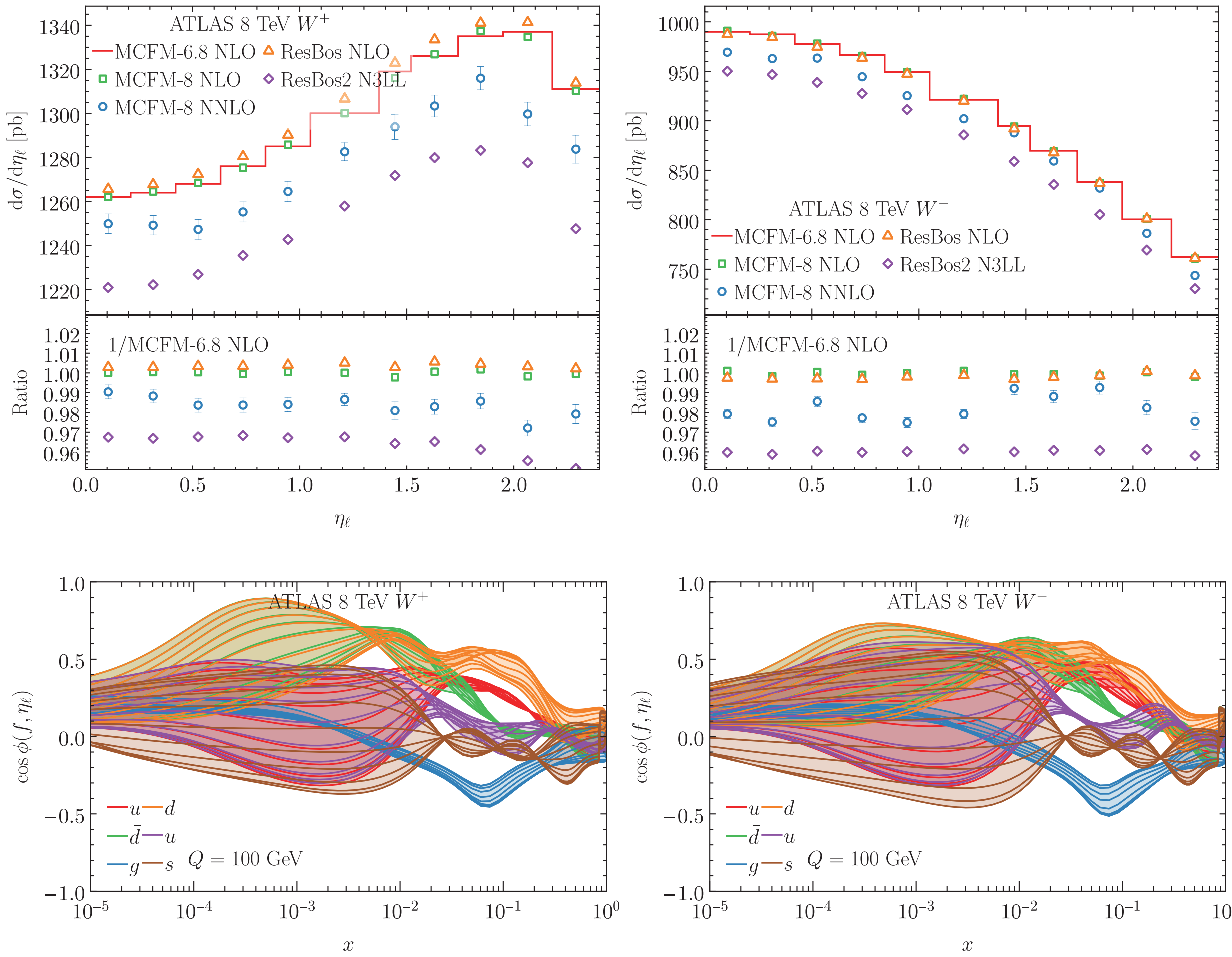

FIG. 2. Similar to Fig. 1, but for the ATLAS 8 TeV W data.

(iv) *CMS13Z*. The differential cross sections for Z-boson production at the LHC 13 TeV were measured by the CMS Collaboration with an integrated luminosity of 35.9 fb^{-1} [85], which is denoted as CMS13Z in this work. The fiducial phase space requires leptons to have $p_T^\ell > 25$ GeV, $|\eta_\ell| < 2.4$ and $|m_{\ell\ell} - M_Z| < 15$ GeV. The data were presented in terms of one-dimensional distributions of rapidity y_Z, transverse momentum p_T^Z, and the optimized angular variable ϕ_η^{*}[3] of the lepton pairs, respectively. The double differential distribution in terms of (y_Z, p_T^Z) was also presented. In this study, we will mainly focus on the rapidity distribution, while other distributions are left for a future study that focuses on the vector-boson transverse momentum (p_T) distributions. In Fig. 4, we display our theoretical predictions and the correlation cosine, which shows a large correlation to the strangeness PDF, while anticorrelation to the $u(\bar{u})$ PDFs.

(v) *LHCb8W*. The $W \to e\nu$ production at the 8 TeV LHC 8 in the forward region was measured by the LHCb with an integrated luminosity of 2 fb^{-1} [88]. We name this dataset as LHCb8W in this work. The fiducial region is defined as $2.0 < \eta < 4.25$ and $p_T^e > 20$ GeV, without additional requirements on the missing energy or transverse mass. The data were presented as differential cross section and charge ratio as a function of the electron pseudorapidity. In this study, we focus on the absolute differential cross sections. The CT18 predictions on the LHCb 8 TeV W production cross section and the correlation cosine are shown in Fig. 5. We note a large variation of various theory predictions for the forward boundary bins, such as the last ones in the upper panels of Fig. 5. This arises mainly because the boundary phase space constrains the Monte Carlo statistics and results in a large theoretical uncertainty. At a higher order, the opening up of new phase space will yield a large QCD correction. As explored later, the inclusion of the boundary bins

---

[3] The optimized angular variable is defined as $\phi_\eta^* = \tan(\frac{\pi-\Delta\phi}{2})/\cosh(\Delta\eta)$, where $\Delta\eta$ and $\Delta\phi$ are the difference in pseudorapidity and azimuthal angle between the two leptons [86]. It probes similar physics as the boson transverse momentum, but with a better experimental resolution [87].

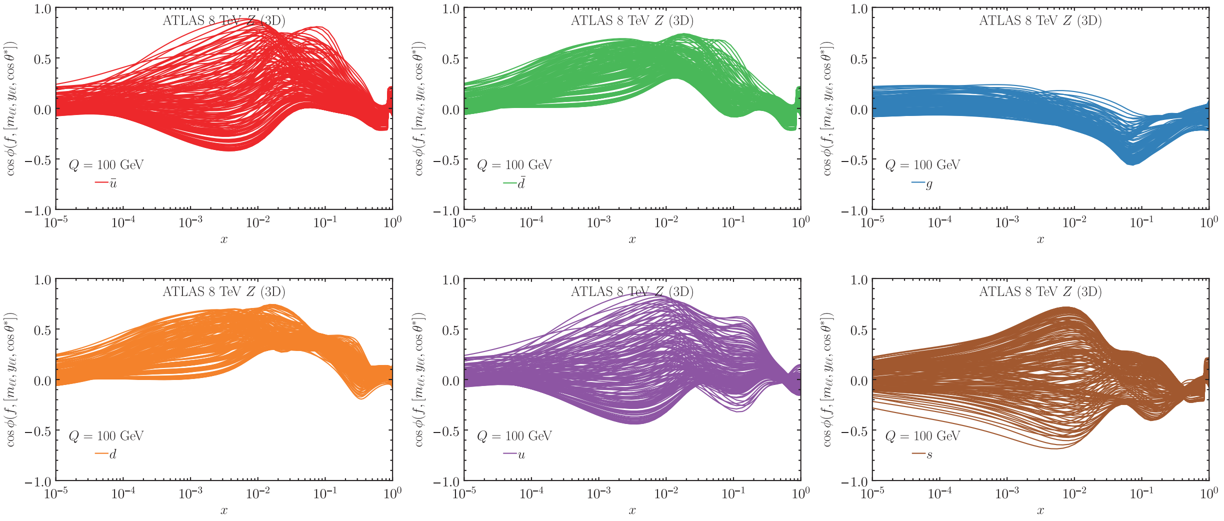

FIG. 3. The correlation cosines between the CT18 PDFs and the ATLAS 8 TeV Z 3D data.

will lead to very poor fits. Therefore, we will exclude them from our canonical fits.

The correlation cosines of the LHCb 8 TeV W data show similar behavior as the ATLAS 8 TeV W data. However, the sensitive x value becomes smaller as a result of the exponential suppression in $x \sim (M_W/\sqrt{s})e^{-y}$, for being produced at the forward (pseudo)rapidity region.

(vi) *LHCb13Z.* The forward Z-boson production in the 13 TeV pp collision in both electron and muon decay channels were measured by the LHCb Collaboration, with an integrated luminosity 0.29 fb^{-1} [89], which we name as LHCb13Z. The fiducial volume is defined as $2.0 < \eta_\ell < 4.5$, $p_T^\ell > 20$ GeV, and $60 < m_{\ell\ell} < 120$ GeV. The differential cross sections were measured in terms of the rapidity, transverse momentum, and optimized angular variable ϕ^*_η. Afterward, the muon-decay channel data were updated with a higher-integrated luminosity, 5.1 fb^{-1} [90]. Our theoretical predictions as well as the correlation cosines are shown in Fig. 6. Similarly, we obtain large uncertainty for the boundary bins (the first and last ones), which will be excluded in our canonical fits. In comparison with the CMS 13 TeV data, the LHCb 13 TeV Z data show stronger correlations to the $u(\bar{u})$ and $d(\bar{d})$ PDFs in the small-x region.

As to be discussed below, the CT18 PDFs can describe the lower-luminosity data [89] very well as a result of the relatively large statistical uncertainty, with χ^2/N_{pt} shown in Table II. In another word, this dataset has a very limited impact on our global fit.

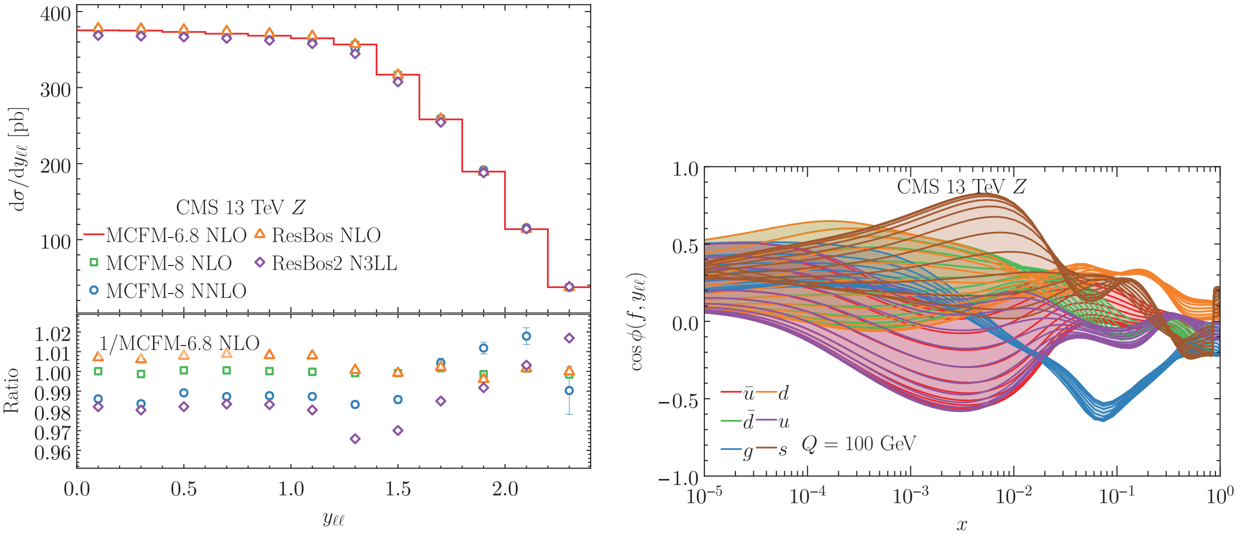

FIG. 4. Similar to Fig. 1, but for the CMS 13 TeV Z data.

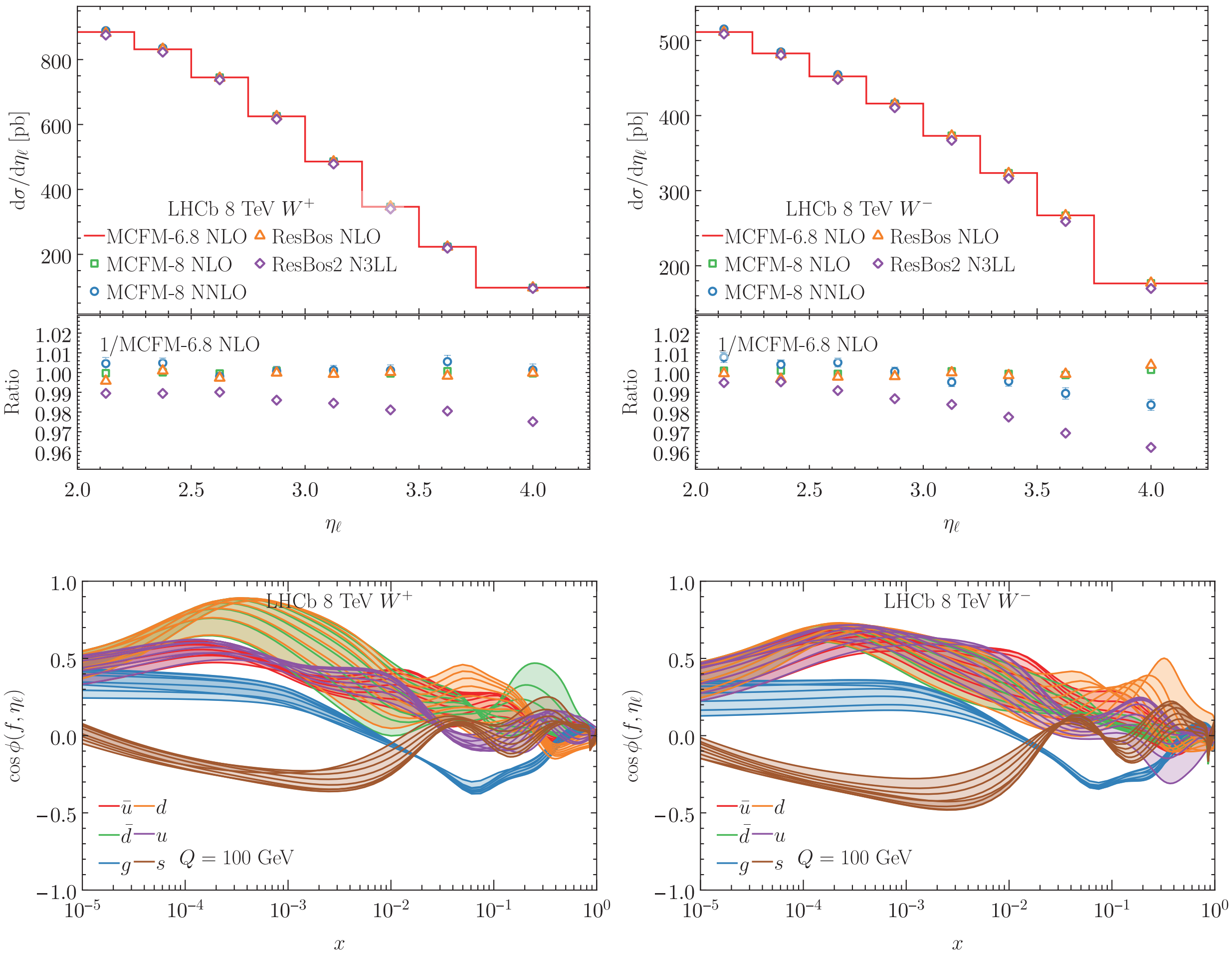

FIG. 5. Similar to Fig. 1, but for the LHCb 8 TeV W data.

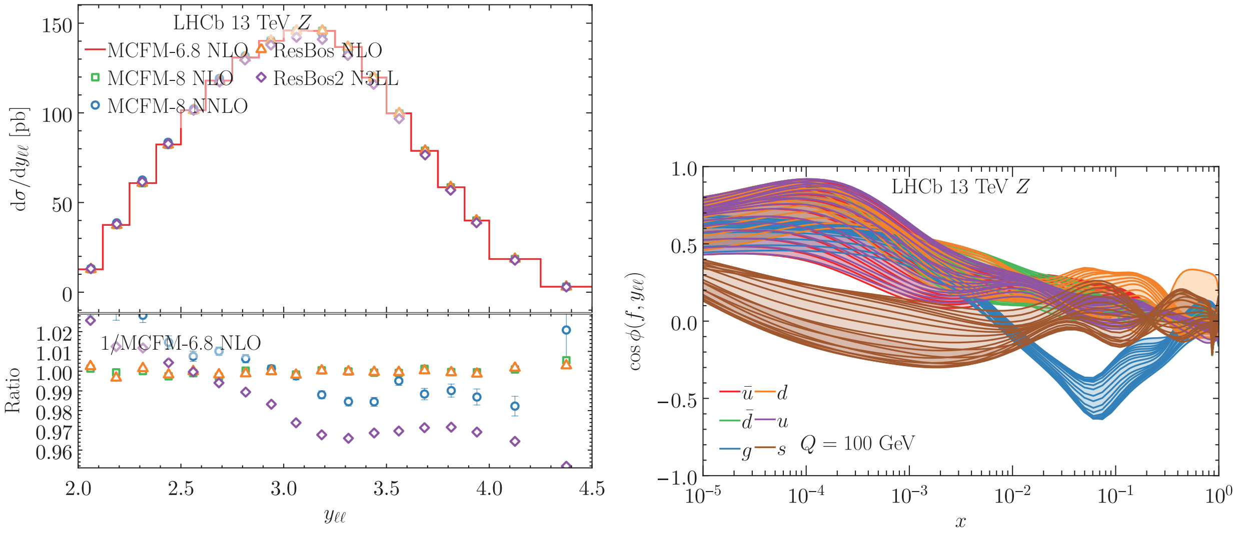

FIG. 6. Similar to Fig. 1, but for the LHCb 13 TeV Z data.

TABLE I. Comparison of the χ^2/N_{pt} for the Drell-Yan (W/Z) data inlcuded in the CT18 [14], MSHT20 [15], and NNPDF3.1 [16], 4.0 [17] global analyses. The numbers in the parentheses indicate the data points.

Data	$\sqrt{s}$ (TeV)	$\mathcal{L}_{\mathrm{int}}$ (fb^{-1})	Ref.	CT18	MSHT20	NNPDF3.1	NNPDF4.0	ATLASpdf21
ATLAS								
Low-mass DY $m_{\ell\ell}$	7	1.6	[91]			0.90(6)	0.88(6)	
High-mass DY $m_{\ell\ell}$	7	4.9	[92]		1.45(13)	1.54(5)	1.68(5)	
W, Z	7	0.035	[72]		1.0 (30)	0.96(30)	0.98(30)	
W, Z	7	4.6	[93]		1.91(61)	2.14(34)	1.67(61)	1.24(55)
$Z(p_T, y_Z)$	7	4.7	[94]					
W	8	20.2	[80]	4.96(22)	2.61(22)		[3.50](22)	1.40(22)
High-mass DY $(m_{\ell\ell}, y_{\ell\ell})$	8	20.3	[95]		1.18(48)		1.11(48)	
$Z(m_{\ell\ell}, y_{\ell\ell}, \cos\theta^*)$	8	20.2	[81]	1.95(188)	1.45(59)		1.22 (60)	1.13(184)
$Z(p_T, m_{\ell\ell})$	8	20.3	[96]			0.93(44)	0.91(44)	
$Z(p_T, y_Z)$	8	20.3	[96]	1.1(27)	1.81(104)	0.94(48)	0.90(48)	
$\sigma^{\mathrm{tot}}_{W,Z}$	13	0.081	[97]				0.80(3)	
$W, Z\sigma^{\mathrm{fid,tot}}$	2.76	0.004	[98]					
W, Z	5.02	0.025	[78]	1.15(27)				
$Zp_T^{\ell\ell}$	13	36.1	[99]					
CMS								
W asym	7	0.036	[100]		0.31(24)			
Z	7	0.036	[101]		0.51(35)			
WA_e	7	0.84	[71]	0.4(11)	0.70(11)	0.78(11)	0.84(11)	
WA_μ	7	4.7	[70]	0.7(11)		1.75(11)	1.70(11)	
$W \to \mu\nu$	8	18.8	[102]	1.0(11)	0.58(22)	1.0(22)	1.38(22)	
DY $Z(m_{\mu\mu}, y_{\mu\mu})$	7	4.5	[103]		1.09(132)	1.27(110)	1.36(110)	
DY $Z(p_T, y_{\ell\ell})$	8	19.7	[104]		Poor fit	1.32(28)	1.41(22)	
$Z\phi^*, (y_{\ell\ell}, \phi^*)$	8	19.7	[105]					
Zy_Z, p_T, ϕ^*_η	13	35.9	[85]	9.24(12)				
$Wy_W, A_W, (\eta_\ell, p_T^\ell), A_\ell$	13	35.9	[106]					
$Z(m_{\ell\ell})$	13	2.8	[107]					
LHCb								
$Z \to ee$	7	0.94	[108]		2.52(9)	1.49(9)	1.65(9)	
$W, Z \to \mu$	7	0.037	[69]		1.25(10)			
$W, Z \to \mu$	7	1.0	[73]	1.6(33)		1.76(29)	1.97(29)	
$W, Z \to \mu$	8	2.0	[109]	2.1(34)		1.37(30)	1.42(30)	
$W, Z \to \mu$	$7 + 8$		[73,109]		1.48(67)			
$Z \to ee$	8	2.0	[110]	1.0(17)	1.54(17)	1.14(17)	1.33(17)	
$W \to e$	8	2.0	[88]	1.52(14)			[2.61](8)	
$Z \to ee$	13	0.294	[89]	1.58(17)			1.72(15)	
$Z \to \mu\mu$	13	5.1	[89]	0.89			0.99(16)	
$Z \to \mu\mu$	13	5.1	[90]	1.27(16)				

In contrast, the updated one with higher luminosity [90] can provide reasonable constraints on PDFs. For this reason, we will only include the updated data in our canonical analysis.

We summarize all these new LHC Drell-Yan datasets as well as those included in the previous CT18 PDF fit [14] in Table I. Meanwhile, we also compare the fitting quality χ^2/N_{pt} and the corresponding number of data points included in the global analyses of the MSHT20 [15], NNPDF3.1 [16], and NNPDF4.0 [17].

In this study, we will not consider the high-mass Drell-Yan data, such as ATLAS 7 TeV [92] and CMS 13 TeV [107] invariant mass of the dilepton pair $(m_{\ell\ell})$ distribution, the ATLAS 8 TeV [95] and CMS 7 TeV [103] double differential $(m_{\ell\ell}, y_{\ell\ell})$ distribution. A good description of these datasets requires the inclusion of EW corrections, which incorporates photon as a parton content [22]. This will be left for a future study on updating the photon PDF of the proton. Furthermore, we do not consider the transverse momentum distribution of Z boson either. As studied in Ref. [48] and references therein, the low p_T^Z data requires a q_T resummation calculation, which involves a nonperturbative transverse-momentum-dependent (TMD) parameter determination. The high p_T^Z data suffer a large EW correction as studied in the CT18 analysis [14]. We leave these aspects to future dedicated studies.

TABLE II. Comparisons of χ^2/N_{pt} for the post-CT18 LHC Drell-Yan data which are included one by one in the fit. The numbers in the parentheses correspond to the case when including all the LHCb data points, while the outside ones are for the case when excluding two boundary bins of the LHCb data.

			χ^2/N_{pt}				
ID	Experiment	N_{pt}	Prefit[a]	ePump[a]	CT18	CT18A	CT18As
215	ATLAS 5.02 TeV *W*, *Z*	27	1.15	0.96	1.07	0.74	0.71
211	ATLAS 8 TeV *W*	22	4.96	2.98	2.46	2.72	2.49
214	ATLAS 8 TeV *Z* 3D	188	1.95	1.18	1.16	1.13	1.14
212	CMS 13 TeV *Z*	12	9.24	2.93	2.75	1.89	2.02
216	LHCb 8 TeV *W*	(16)14	(3.48)1.52	(3.24)1.45	(2.81)1.33	(1.89)1.45	(3.00)1.52
	LHCb 13 TeV *Z*	18	0.89	0.88	0.99	0.92	0.90
213	LHCb 13 TeV $Z \to \mu^+\mu^-$	(18)16	(2.39)1.27	(2.33)1.17	(2.55)1.12	(2.49)1.12	(2.28)0.87

[a] The χ^2/N_{pt} values for the prefit and ePump are based on the CT18 PDFs.

III. IMPACTS ON THE CT18 PDFS

Before performing global fits with the inclusion of all these post-CT18 LHC Drell-Yan datasets simultaneously, we would like to examine the impact of the individual dataset on the CT18 PDFs. This can be done by performing the ePump updating [67,68] or a global fitting by including one new dataset at a time on the top of CT18. Note that the CT18 + ATL7WZ fit is the same as the CT18A which includes the ATLAS 7 TeV *W*, *Z* precision dataset (named as ATL7WZ) [93]. The comparisons of χ^2/N_{pt} from CT18's prefit, ePump updating and global fitting are summarized in Table II.

In comparison with the ePump updating, in general, the χ^2/N_{pt} decreases slightly in the global fitting, reflecting the non-negligible impact of these new datasets. Two exceptions happen to the ATL5WZ and LHCb13Z datasets, due to the pull of other datasets in the global fitting. Nevertheless, both datasets can be well-described by CT18 with χ^2/N_{pt} about 1. Considering the prefit values of $\chi^2/N_{\text{pt}} \sim 1$, the impact of these two datasets is expected to be minimal, which will be illustrated later.

For comparison, we also present the global fitted χ^2/N_{pt} with the setup of CT18A and CT18As in Table II. Recall that CT18A is CT18 with the inclusion of ATL7WZ precision data which shows sizable tension with other datasets, such as the HERA I + II combined data and neutrino DIS dimuon data [14]. On top of CT18A, the CT18As fit includes more degrees of freedom in the strangeness parametrization to allow s not equal to $\bar{s}$ at the initial scale $Q_0 = 1.3$ GeV which relaxes the above mentioned tension [66]. In comparison with the fitted CT18 χ^2/N_{pt}, we see the fitted CT18A ones generally have smaller values, suggesting the consistency between the ATL7WZ with these new DY datasets. In contrast, the χ^2/N_{pt} for the ATL8W data increases from 2.46 to 2.72, as an indication of some tension. With a more flexible strangeness parametrization in CT18As, this tension can be relaxed down to $\chi^2/N_{\text{pt}} = 2.49$. A minor increase of χ^2/N_{pt} value is observed when using the LHCb8W data to update CT18As as compared to CT18 and CT18A. But, considering the small variation with respect to the ATL8W one, the impact of LHCb8W is expected to be small, which will be examined more closely later.

In Fig. 7, we show the ePump updated and the global fitted $\bar{d}, g, s$ PDFs at $Q = 100$ GeV, as an example to demonstrate the impact of post-CT18 LHC Drell-Yan datasets on the CT18 PDFs. A similar comparison for other PDF flavors is collected in Fig. 15 of Appendix. Here, we also include the reference PDF error bands for the CT18 + ATL7WZ fit, i.e., CT18A, while only central PDFs for other fits.

As shown in Fig. 7, the ATL7WZ dataset in the CT18A fit softens the $\bar{d}$ PDF, but enhances the $s(\bar{s})$ PDF at x around 10^{-3}–10^{-2}. Most of the post-CT18 LHC Drell-Yan datasets also prefer larger $s(\bar{s})$ PDF than what CT18 predicts, implying consistency with the ATL7WZ data. The strongest impacts come from the ATL8Z3D and CMS13Z data, even though the strength are milder than ATL7WZ data. In comparison with the fitted PDFs, the ePump updated ones give similar results, with only slightly smaller pulls for CT18 + CMS13Z $s(x)$ PDF, as a result of the limitation of the Hessian linear approximation [14,67].

However, by looking at the $\bar{d}$ PDF, we realize that both the ATL8W and LHCb8W data pull the CT18 $\bar{d}$ PDF to the opposite direction at x around $\sim 10^{-3}$, with respect to ATL7WZ and other post-CT18 LHC Drell-Yan data. It suggests a tension of the ATL8W (and LHCb8W) data with other datasets, such as ATL8Z3D. We also note that when the LHCb8W data is included to update the CT18 PDFs, cf. Fig. 7, an opposite pull on $\bar{d}$ PDF occurs at $x \sim 0.3$ where the PDF uncertainty is large.

IV. GLOBAL FITS

A. χ^2 and PDFs for individual flavors

Now, we can simultaneously fit these new post-CT18 LHC Drell-Yan datasets (denoted as "CT18 + nDY", etc.)

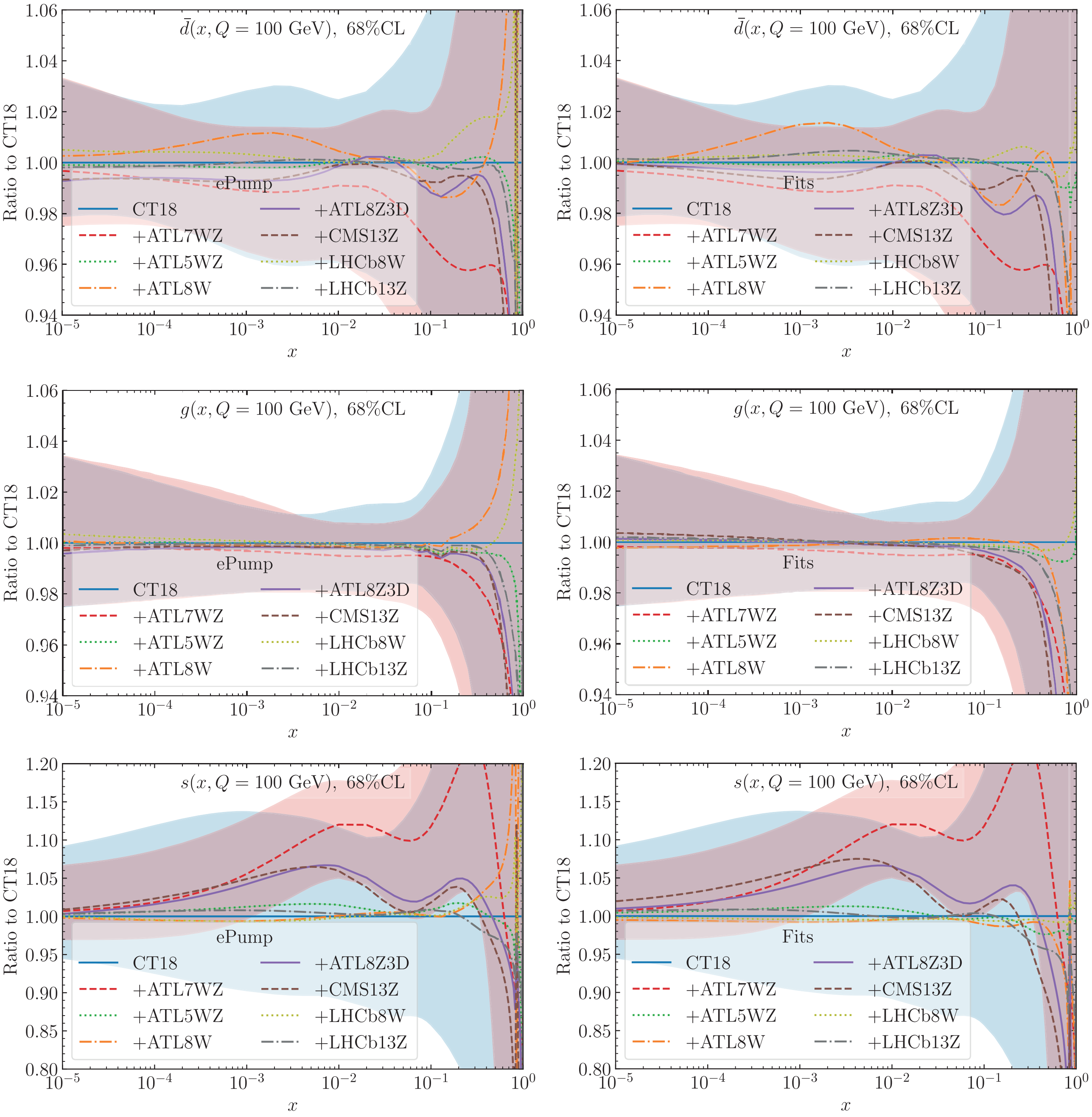

FIG. 7. The impact of post-CT18 LHC Drell-Yan datasets on updating the CT18 $\bar{d}$ and s PDFs at $Q = 100$ GeV, by including the individual dataset one by one with the ePump (left) and global fitting (right). The two error bands correspond to the CT18 and CT18 + ATL7WZ = CT18A PDFs, respectively.

to study their impact on the CTEQ-TEQ PDFs. Within the CT18, CT18A, and CT18As framework, we present the corresponding fitted χ^2/N_{pt} for each of the post-CT18 LHC Drell-Yan dataset and the combined datasets in Table III. We included the ATL7WZ data set as well in this comparison. As discovered already in the individual fits, the χ^2 for each set follows the same trend as Table II. That is to say, except for the ATLAS and the LHCb 8 TeV W datasets, the χ^2 decreases from CT18 to CT18A, and to CT18As, reflecting the general consistency among these datasets. The χ^2/N_{pt} values of ATL8W and LHCb8W increase from updating CT18 to CT18A, as a result of the tension with the ATL7WZ data. The updated CT18As can reduce the χ^2 for these two sets, due to the additional degree of freedom in the s and $\bar{s}$ PDFs.

We compare the fitted PDFs for sea quarks $\bar{u}, \bar{d}$ and s at $Q = 100$ GeV, before and after including the post-CT18 LHC Drell-Yan datasets in Fig. 8, and the comparisons for

TABLE III. Similarly to Table II, but with global fits by including the post-CT18 LHC Drell-Yan datasets simultaneously. We include the MSHT20 [15], NNPDF4.0 [17] and ATLASpdf21 [18] results for comparison.

			$\chi^2/N_{\rm pt}$					
ID	Experiment	$N_{\rm pt}$	CT18	CT18A	CT18As	ATLASpdf21	MSHT20	NNPDF4.0
215	ATLAS 5.02 TeV W, Z	27	0.81	0.71	0.71	…	…	…
211	ATLAS 8 TeV W	22	2.45	2.63	2.51	1.41	2.61	[3.50]
214	ATLAS 8 TeV Z 3D[a]	188	1.12	1.14	1.18	1.13(184)	1.45(59)	1.22(60)
212	CMS 13 TeV Z	12	2.38	2.03	2.71	…	…	…
216	LHCb 8 TeV W	14	1.34	1.36	1.43	…	…	…
213	LHCb 13 TeV Z	16	1.10	0.98	0.83	…	…	…
248	ATLAS 7 TeV W, Z	34	2.52	2.50	2.30	1.24(55)	1.91(61)	1.67(61)
Total 3994/3953/3959 points			1.20	1.20	1.19	…	…	…

[a] Different from ATLASpdf21 [18] and our treatment of the ATLAS 8 TeV Z data, i.e., directly fitting the triple differential distributions of $(m_{\ell\ell}, y_{\ell\ell}, \cos\theta^*)$, MSHT20 and NNPDF4.0 have summed over the $\cos\theta^*$ bins and resulted in double-differential distributions of $(m_{\ell\ell}, y_{\ell\ell})$ with the number of data points indicated in parentheses, respectively.

other light flavors g, u, and d are shown in Fig. 9. We display the flavor singlet $\Sigma = \sum_i (q_i + \bar{q}_i)$ in Fig. 16 of Appendix. Recall that the ATL7WZ data in the CT18A fit enhances the $s(\bar{s})$ PDFs but reduces the $d(\bar{d})$, which is shown again in Fig. 8. In comparison, the post-CT18 Drell-Yan datasets in the "CT18 + nDY" fit pull the strangeness in the same direction but with a milder distance. The "CT18A + nDY" accumulates both the impacts from ATL7WZ and post-CT18 LHC Drell-Yan datasets. However, when examining the $d(\bar{d})$ flavor more carefully, we see that the post-CT18 LHC Drell-Yan data pull CT18 PDFs in the opposite direction with respect to the CT18A PDFs. This behavior shows up already in the individual fits as shown in Fig. 7. It is driven by the tension between the ATL8W data and ATL7WZ data. The inclusion of ATL7WZ and post-CT18 LHC Drell-Yan datasets in the CT18A + nDY fit yields $d(\bar{d})$ PDFs lying in between CT18 + nDY and CT18A, as a consequence of the tension between ATL7WZ and "nDY" datasets.

In comparison with the CT18A, the additional freedom of the $s(\bar{s})$ PDFs in CT18As allows the $s(\bar{s})$ to be pulled further [66]. As a result, the ATL8Z3D $\chi^2/N_{\rm pt}$ can increase slightly, as shown in Table III, indicating that the relaxed tension mentioned above is not completely resolved. Under such an assumption, the impacts of the post-CT18 LHC Drell-Yan datasets on the $s(\bar{s})$ PDFs, as well as other flavors, becomes minor in most scenarios, with only a mild enhancement of the $d(\bar{d})$ PDFs around $x \sim 10^{-3}$, as shown in Figs. 8 and 9. The impacts of all these Drell-Yan datasets on the gluon PDF is limited, which contributes through higher-order corrections to the Drell-Yan process. Details of the comparison can be found in Fig. 9.

We also include the comparison of the $\bar{d}$ and s PDF error bands in Fig. 8. Starting with strangeness, we see the ATL7WZ dataset shrinks the PDF error band in the $x \in [10^{-4}, 10^{-1}]$ range. A similar impact can be obtained with the post-CT18 LHC Drell-Yan datasets, shown as the error band of "CT18 + nDY", which imposes a slightly stronger constraint around $x \sim 10^{-2}$ as a result of including more data. The impacts from both ATL7WZ and post-CT18 LHC Drell-Yan datasets are combined in the "CT18A + nDY". With the additional freedom of strangeness asymmetry in CT18As, the $s(\bar{s})$ PDF error band becomes larger in comparison with the CT18A. Under such a scenario, the change of the strangeness error band due to the post-CT18 LHC Drell-Yan datasets is quite limited.

When examining the $d(\bar{d})$ flavor, the CT18A shrinks the error bands in the range of $x \in [10^{-4}, 10^{-2}]$. The post-CT18 LHC Drell-Yan datasets play the same role as ATL7WZ data in CT18A, which yields a similar error band to "CT18 + nDY" as the CT18A. Under such a condition, the accumulation of post-CT18 LHC Drell-Yan datasets only contributes a minor reduction of the error band in the range $x \in [10^{-3}, 10^{-1}]$ in the negative direction of Hessian asymmetric errors. Similar to the strangeness PDF, the additional freedom in CT18As enlarges the $d(\bar{d})$ error bands. On top of CT18As, the inclusion of the post-CT18 LHC Drell-Yan datasets can reduce the PDF error bands.

B. Flavor ratios and strangeness asymmetry

Besides the individual flavors, we also examine the impact of the post-CT18 LHC Drell-Yan datasets on the flavor ratios d/u, $\bar{d}/\bar{u}$, as well as $R_s = (s + \bar{s})/(\bar{d} + \bar{u})$ in Fig. 10. The flavor difference $x(\bar{d} - \bar{u})$ and ratio $(\bar{d} - \bar{u})/(\bar{d} + \bar{u})$ are left in Fig. 17 of Appendix. Instead of a high scale such as $Q = 100$ GeV, here we show them at the starting scale $Q_0 = 1.3$ GeV, which shows a more pronounced effect from the post-CT18 LHC Drell-Yan

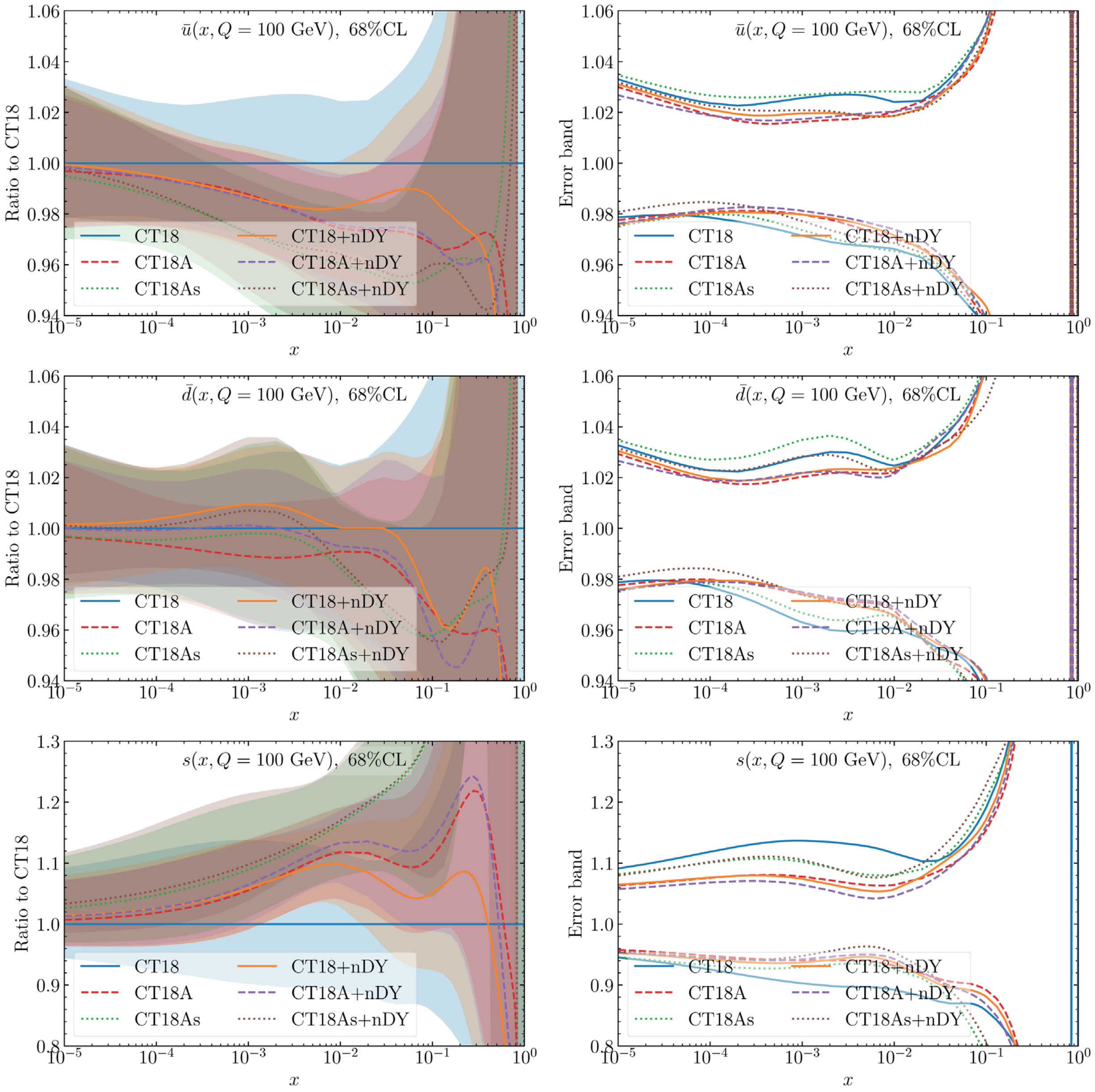

FIG. 8. Comparison of $\bar{u}$, $\bar{d}$, and s PDFs at $Q = 100$ GeV for various fits.

datasets. The main features can be deduced from the individual flavors already shown in Figs. 8 and 9. For example, the post-CT18 LHC Drell-Yan data enhance the $R_s = (s + \bar{s})/(\bar{d} + \bar{u})$, with the extent slightly smaller than the impact of the ATL7WZ in CT18A. Both impacts are accumulated in the CT18A + nDY sets. With a more flexible parametrization of strangeness PDFs in CT18As, the impact of post-CT18 LHC Drell-Yan data is quite minimal. The inclusion of the post-CT18 LHC Drell-Yan data gives an enhancement to the d/u and $\bar{d}/\bar{u}$ ratios at $x \sim 10^{-3}$ as shown in Fig. 10 and similarly to $x(\bar{d} - \bar{u})$ and $(\bar{d} - \bar{u})/(\bar{d} + \bar{u})$ in Fig. 17, which mainly originates from the ATL8W's modification to the $d(\bar{d})$ PDF. This feature is different from the CT18A, of which the d/u and $\bar{d}/\bar{u}$ ratios at $x \sim 10^{-3}$ are more or less the same as CT18, after the inclusion of ATL7WZ data. The impact on the ratio uncertainties can be understood similarly.

Finally, we compare the R_s as well as the strangeness asymmetry $s_-(x) = s(x) - \bar{s}(x)$ among the CT18As(+Lat[4] [66]/nDY), MSHT20, and NNPDF4.0 in Fig. 11. We remind that the CT18As + Lat fit [66] includes additional lattice data [111], which constrain the strangeness asymmetry in the large x region. Similar to the s PDF in Fig. 8 or R_s ratio in Fig. 10, the post-CT18 LHC Drell-Yan datasets

---

[4] Throughout this work, we use the notation CT18As + Lat to represent the CT18As_Lat fit presented in Ref. [66], for convenience.

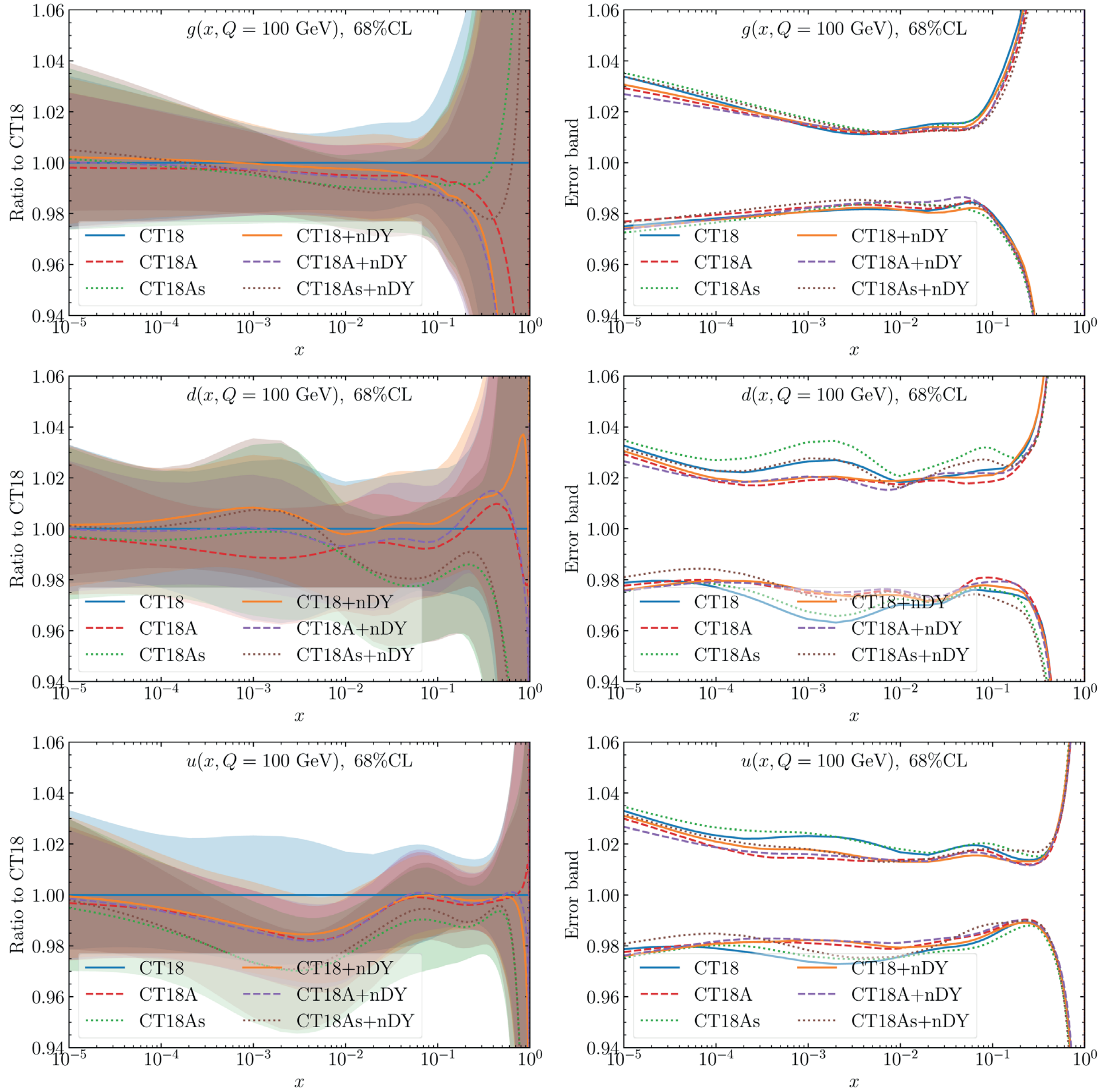

FIG. 9. Similar to Fig. 8, but for g, d, and u PDFs at $Q = 100$ GeV.

give a very minor impact on the strangeness asymmetry, both with and without the lattice data. Both MSHT20 and NNPDF4.0 give softer R_s ratios than CT18(+nDY), with an overall agreement within the corresponding error band. As emphasized in Ref. [66], the inclusion of the lattice s_- data in the CT18As + Lat fit gets modifications on both the central fit and the error bands of R_s and $s_-(x)$, as shown in Fig. 11. The R_s of CT18As + Lat gets closer to that of MSHT20 and NNPDF4.0, while the strangeness asymmetry s_- of CT18As is closer to zero at large x than that of MSHT20 and NNPDF4.0, due to the constraint from the lattice data. Furthermore, this conclusion remains when the post-CT18 LHC Drell-Yan (nDY) data is included in various CT18As(+Lat) global fits.

C. Data descriptions

In Fig. 12, we compare the theoretical predictions for the ATLAS 5.02, 7, and 8 TeV W, Z productions from the CT18, CT18A, and CT18As fits before and after including the post-CT18 LHC Drell-Yan data. We provide similar comparisons for the ATL8Z3D, CMS13Z, and LHCb data in Figs. 18–20 of Appendix, respectively. Here, we show the raw data, instead of the shifted ones, as the systematical shifts vary in terms of the corresponding fitted PDFs. As we expected, the general agreement of the fits with experimental data becomes better after the inclusion of these post-CT18 LHC Drell-Yan datasets. Meanwhile, the degree of impact of each dataset usually depends on both the degree of agreement before the fit as well as the size of uncorrelated uncertainty (quadrature sum

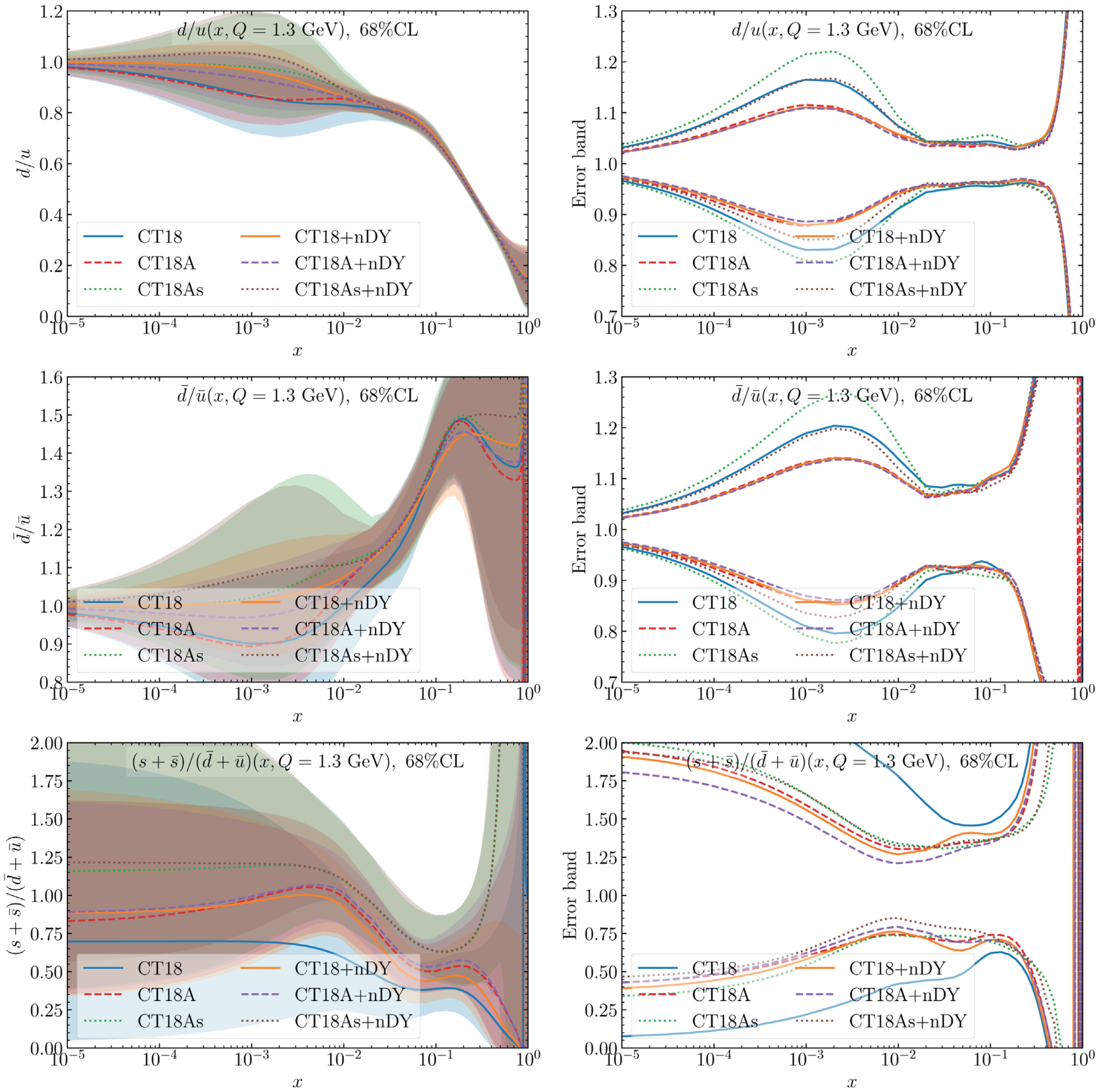

FIG. 10. Similar to Fig. 8, but for the flavor ratios $d/u, \bar{d}/\bar{u}$ and $R_s = (s+\bar{s})/(\bar{d}+\bar{u})$ at $Q = 1.3$ GeV.

of the statistical and uncorrelated systematical uncertainties) of the data. For example, we obtain a significantly larger pull on the $d(\bar{d})$ PDFs from the ATL8W data, with respect to the ATL5WZ, mainly driven by the smaller uncorrelated uncertainties, as shown in Fig. 12. Of course, the number of data points makes a difference as well, such as in the ATL8Z3D case as shown in Fig. 18.

Also, we observe that the theoretical predictions of these Drell-Yan data are generally smaller than the experimental data, It suggests an overall consistency among these datasets, which results in the same directional pulls, e.g., enhancing s-PDF at x around 10^{-3}, as shown in Fig. 7. As we know in terms of the correlation cosine, the pull of W production is mainly reflected on the $d(\bar{d})$ and $u(\bar{u})$ PDFs. As a consequence, the ATL8W data will lift the d and $\bar{d}$ PDFs upwardly, as shown in Figs. 7 and 15, respectively. However, this does not show up in the ATL7WZ data, due to the different pull of the Z data.

In comparison with the ATL7WZ pull in the CT18A PDFs, we obtain a similar pull on the s PDF from the CMS13Z data, hinted by the similar trend of comparison between the theoretical prediction and experimental data, as shown in Fig. 19. In comparison, the impact of the LHCb 13 TeV Z data is quite minimal. We compare the corresponding theory predictions and data in Fig. 20 for completeness.

D. Phenomenological implications

We present the comparison of the PDF parton luminosities before and after including the post-CT18 LHC

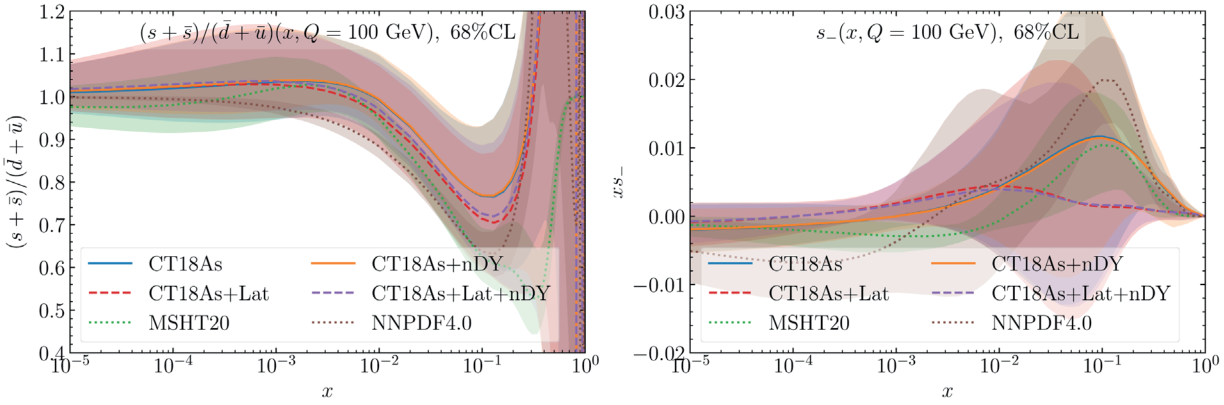

FIG. 11. Lower: Comparison of the ratio $R_s = (s+\bar{s})/(\bar{d}+\bar{u})$ (left) and the strangeness asymmetry $s_- = s - \bar{s}$ (right) of CT18As(+Lat/nDY), MSHT20 and NNPDF4.0 PDFs at $Q = 100$ GeV.

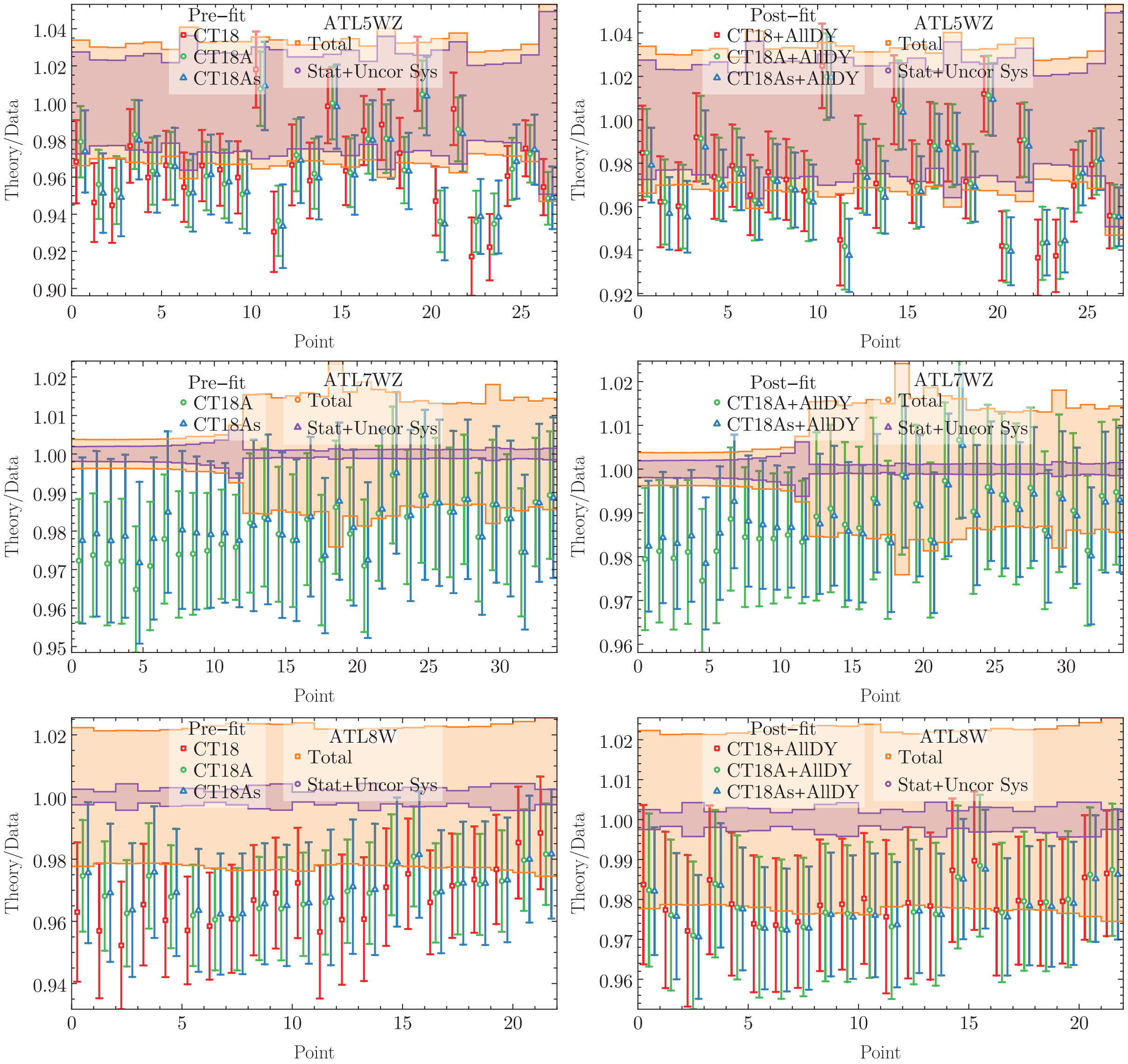

FIG. 12. Comparisons of various theoretical predictions of CT18, CT18A, CT18As PDFs (left) and CT18 + nDY, CT18A + nDY, CT18As + nDY PDFs (right), and the ATLAS 5.02, 7, and 8 TeV W, Z data. The total error of each experimental data point is presented as the shaded yellow band, which is much larger than the sum of statistical and uncorrelated systematic errors in quadrature.

Drell-Yan data in the CT18, CT18A, and CT18As, as well as CT18Z and CT18As + Lat + nDY (accumulating lattice [66] and nDY data) fits in Fig. 13. The parton luminosity is defined as [112]

$$\mathcal{L}_{ij}(s, m_X^2) = \frac{1}{s}\frac{1}{1+\delta_{ij}}\int_\tau^1 \frac{\mathrm{d}x}{x}[f_i(x,Q^2)f_j(\tau/x,Q^2) + (i \leftrightarrow j)], \tag{4}$$

where $\tau = m_X^2/s$, with $\sqrt{s}$ being the center-of-mass energy of the collider, and factorization scale $Q^2 = m_X^2$. Let us recall the parton luminosities of CT18A [14] at low invariant-mass region: (i) the gluon-gluon luminosity ($\mathcal{L}_{gg}$) is reduced; (ii) both the quark-antiquark luminosity ($\mathcal{L}_{q\bar{q}} = \sum_i \mathcal{L}_{q_i\bar{q}_i}$) and the singlet-singlet luminosity ($\mathcal{L}_{\Sigma\Sigma}$) are enhanced; (iii) the gluon-singlet luminosity ($\mathcal{L}_{g\Sigma}$) is almost unchanged. The parton luminosity uncertainties of CT18A are slightly smaller than the CT18.

In comparison with the gg luminosity of CT18 PDFs, the post-CT18 LHC Drell-Yan datasets pull the CT18 + nDY gg luminosity in the same direction as CT18A gg luminosity at low- and high-invariant mass m_X region. However, the amount of change in $q\bar{q}$ luminosity is opposite, i.e., larger (smaller) change at low(high)-invariant mass m_X region. In comparison, the change in the $g\Sigma$ luminosity and $\Sigma\Sigma$ luminosity become larger than the CT18A's difference from CT18. In many cases, the parton luminosities of CT18A + nDY resemble CT18 + nDY, except in the TeV region. Furthermore, the parton luminosities of CT18As + nDY are quite similar to CT18A + nDY. The parton luminosity uncertainties of CT18As + nDY PDFs are slightly larger than CT18A + nDY as a result of additional degrees of freedom in the strangeness PDFs. We also note that the changes from both CT18 PDFs to CT18As + nDY PDFs (e.g., s, g, $\bar{d}$) and the corresponding parton luminosities are quite similar to the changes from CT18 to CT18Z PDFs [14].

As examples of phenomenological implications, we present the correlation ellipses of the LHC 14 TeV fiducial $W^\pm, Z$ and inclusive Higgs boson (H), top-quark pair ($t\bar{t}$), and associated $t\bar{t}H$ productions in Fig. 14, as well as the corresponding correlation cosine to various PDF flavors at $Q = 100$ GeV in Figs. 21 and 22 of Appendix. The fiducial $W^\pm, Z$ cross sections correspond to the same kinematic cuts adopted in the ATLAS 13 TeV measurement [97],

$$\begin{aligned} &W^\pm\!: p_T^{\ell,\nu} > 25\,\mathrm{GeV},\ \ |\eta_\ell| < 2.5,\ \ m_T > 50\,\mathrm{GeV},\\ &Z\!: p_T^{\ell} > 25\,\mathrm{GeV},\ \ |\eta_l| < 2.5,\ \ 66 < m_{\ell\ell} < 116\,\mathrm{GeV}. \end{aligned} \tag{5}$$

The calculation is performed with the NLO APPLgrid [74] with the NNLO K-factors from the MCFM [35]. The Higgs, $t\bar{t}$, and $t\bar{t}H$ productions refer to the full phase space, without decays. The $t\bar{t}$ cross section is calculated with Top++ [113] at NNLO with soft gluons resummed up to the NNLL level and factorization and renormalization scales are set to the top-quark mass m_t. The Higgs boson production is calculated with ggHiggs [114] at N3LO with the threshold resummation up to N3LL, and scale as the Higgs mass m_H. The $t\bar{t}H$ associated production is calculated with MadGraph_aMC@NLO [115] interfacing with PineAPPL fast interpolation grid [116] at the NLO, and the scale as the partonic collision energy $\sqrt{\hat{s}}$.

Taking the CT18 as a reference, we see that both the ATLAS 7 TeV W, Z data and the post-CT18 LHC Drell-Yan datasets pull the $W^\pm$ and Z boson cross sections to a larger value. The correlations in (W^+, W^-) and $(W^\pm, Z)$ are unchanged, with the reduction of corresponding uncertainties, reflecting the change in the quark-antiquark luminosity. In comparison, Higgs, top-quark pair, and associated $t\bar{t}H$ cross sections are pulled to the smaller values, as a result of the reduction of gg luminosity. We also observe the reduction of the error band with respect to the CT18, due to the inclusion of the post-CT18 LHC Drell-Yan datasets in the fits.

Generally speaking, the theory prediction of CT18 + nDY deviates from CT18 in a similar way as how CT18Z deviates from CT18, as shown in Fig. 14. In most cases, the predicted cross sections of CT18As + nDY lie between those of CT18 and CT18Z, except that $\sigma_H(\mathrm{CT18}) > \sigma_H(\mathrm{CT18Z}) > \sigma_H(\mathrm{CT18As + nDY})$. This can be understood by noting the very similar pattern of difference in various flavor PDFs between CT18As + nDY and CT18Z, when comparing to CT18, e.g., s and g PDFs, as shown in Fig. 23 of Appendix. Excluding CT18Z, the CT18As + nDY PDFs generate the largest deviations from the CT18 predictions. As first pointed out in the CTEQ6.6 analysis [117], the mutual dispositions of the $(W^\pm, Z)$ error ellipse, i.e., the top right panel of Fig. 14, can be associated to the differences among the strangeness and gluon PDFs. The direction parallel to the semiminor axis, associated with the relative cross section ratio $R_{Z/W^\pm} = \sigma_Z/\sigma_{W^\pm}$, is most closely identified with the strange PDF, as shown in terms of the correlation cosine in Fig. 22 (left). Meanwhile, the semimajor axis, i.e., the "$\sigma_Z + \sigma_{W^\pm}$" direction, is most related to the gluon PDF, as shown with respect to the correlation cosine in Fig. 22 (right).

When looking closely at the correlation cosines between various cross sections and flavor PDFs in Fig. 21, we realize that the large anticorrelation between the $W^\pm, Z$ cross sections and gluon-PDF happens at $x \sim 10^{-1}$, where a large positive correlation is observed for the $t\bar{t}$ and $t\bar{t}H$ cross sections. In comparison, the biggest correlation between the Higgs cross section and gluon-PDF occurs at a smaller x value, around $x \sim 10^{-2}$. We also present the $(Z, H/t\bar{t})$ correlation ellipses in Fig. 14, which shows a large anticorrelation between the Z and $t\bar{t}$ cross sections. In comparison, the (Z, H) anticorrelation is relatively weaker. Again, after excluding CT18Z, the largest deviation from the CT18 predictions occurs when using the CT18As + nDY PDFs. The inclusion of additional lattice constraint on

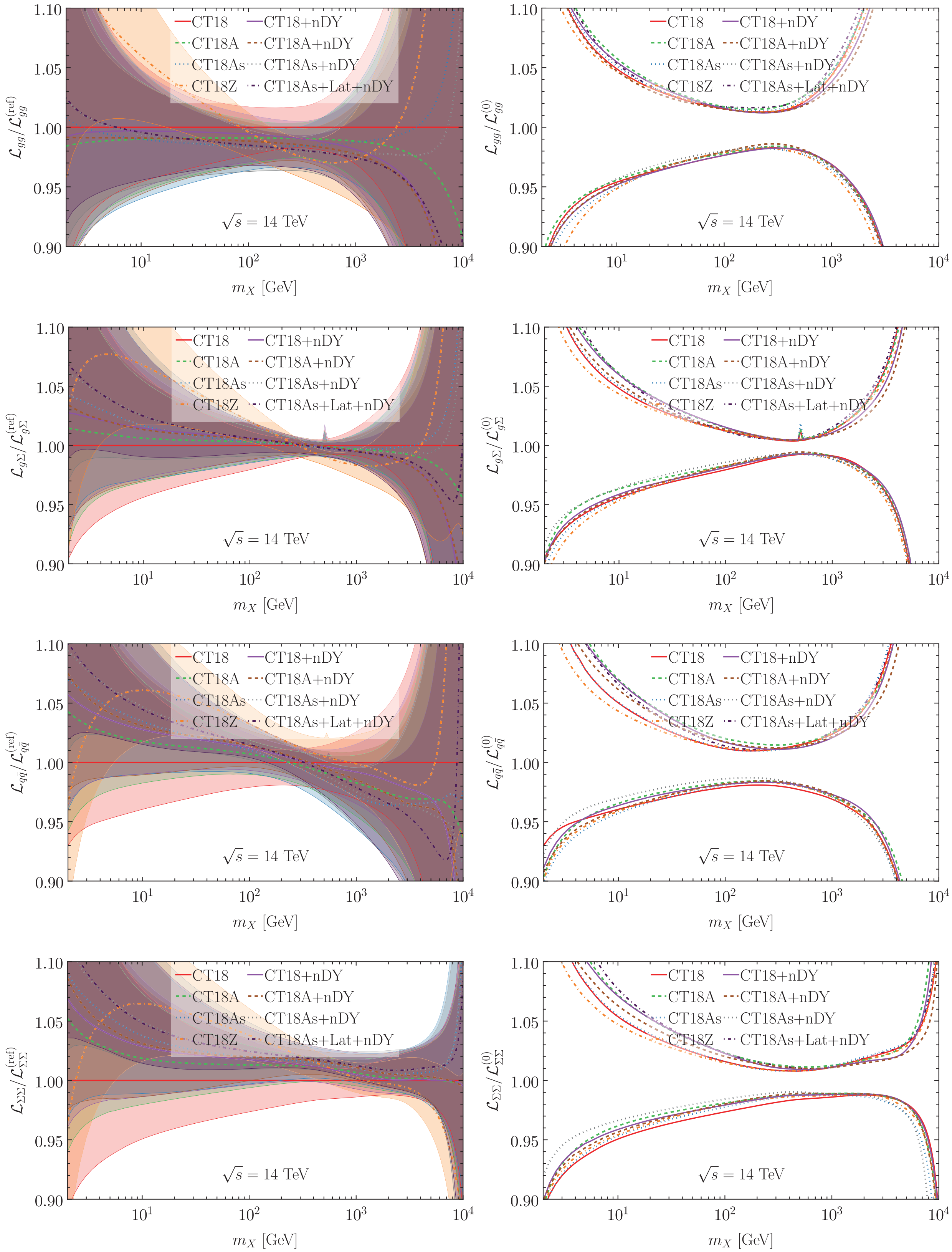

FIG. 13. Comparison of the parton luminosities (left) and and their uncertainties (right) at the 14 TeV LHC, computed with the CT18, CT18A and CT18As PDFs and the PDFs after including the post-CT18 LHC Drell-Yan (nDY) datasets.

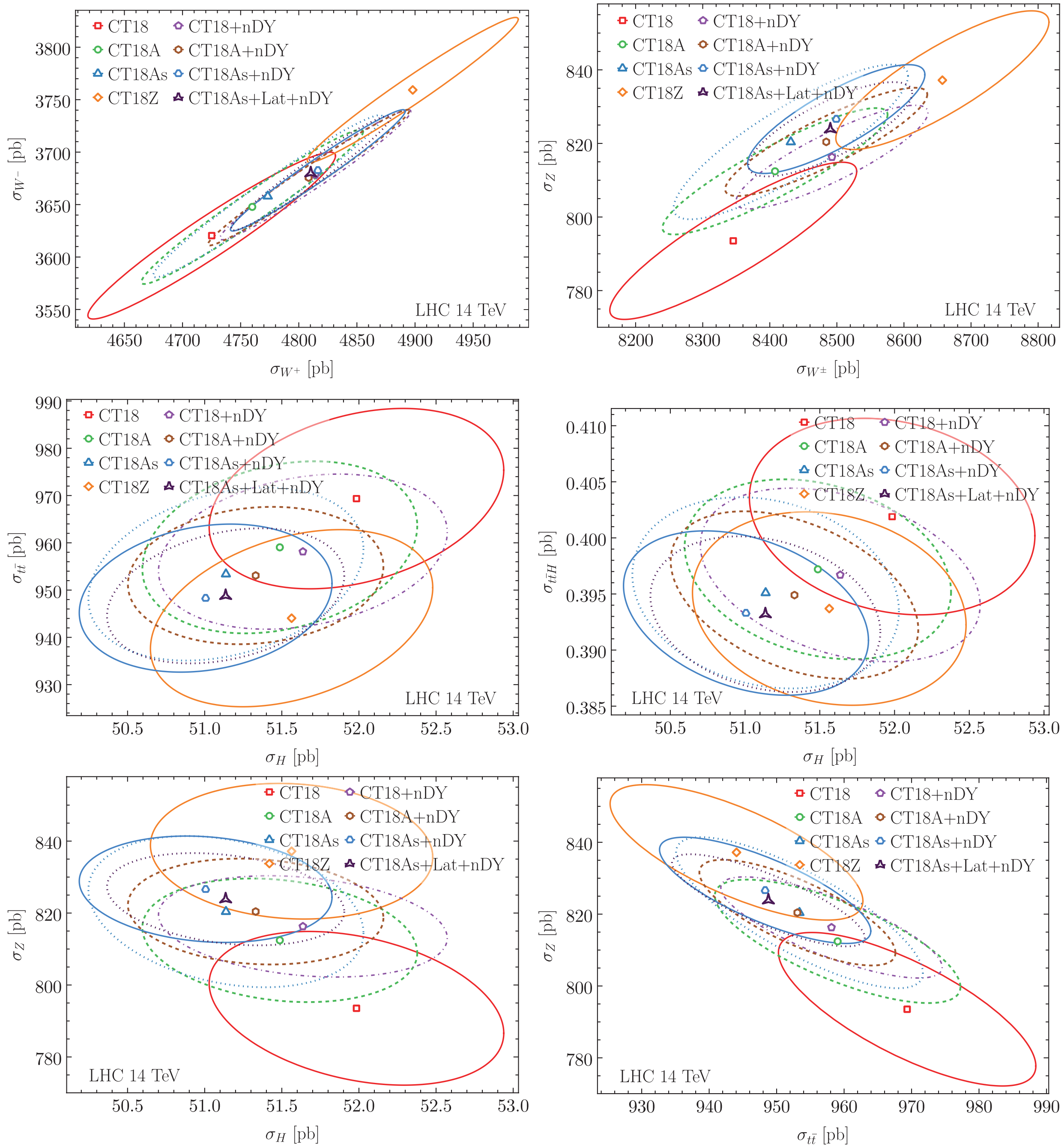

FIG. 14. The 68% C.L. correlation ellipses among the fiducial $W^\pm$, Z and the inclusive H, $t\bar{t}$, and $t\bar{t}H$ productions at the 14 TeV LHC. See the text for its details.

strangeness asymmetry in CT18As + Lat + nDY yields a reduced difference, to a relatively minor extent.

V. DISCUSSION AND CONCLUSION

Since the release of the CT18 family of PDFs [14], a large number of LHC precision data become available. In this work, we perform a detailed study on the impact of the post-CT18 LHC Drell-Yan precision data on the PDFs in the framework of CT18 global analysis.

From the ATLAS measurements, we have considered the 5.02 TeV W, Z production (ATL5WZ) [78], the 8 TeV W production (ATL8W) [80], and the 8 TeV triple differential distribution neutral-current Drell-Yan Z production data $d^3\sigma/(dm_{\ell\ell}dy_{\ell\ell}d\cos\theta^*)$ (ATL8Z3D) [81]. Similarly, we have included the CMS 13 TeV Z boson production (CMS13Z) [85], and the LHCb 8 TeV W boson production (LHCb8W) [88] as well as the 13 TeV Z boson production (LHCb13Z) [89,90]. In this work, we mainly focus on the (pseudo)rapidity distributions around the peak region.

A good description of the high-mass Drell-Yan invariant mass distributions requires the inclusion of the photon PDF to account for the EW corrections as well as the photon initiated process $\gamma\gamma \to \ell^+\ell^-$ [22]. Similarly, the Drell-Yan transverse momentum (p_T) measurements, especially in the low-p_T region, involves the nonperturbative transverse-momentum-dependent (TMD) parton density to account for the effect of multiple soft gluon emissions [48,118–120]. For these reasons, we leave these two types of the measurements for future separate studies.

We have compared the MCFM NNLO fixed order predictions and the ResBos2 matched q_T N3LL resummation calculations for the distributions we considered in this work. The difference is generally at a percent level, as a reflection of the impact of fiducial cuts on different high-order treatments. With a limited computational resource, we generally obtain larger Monte Carlo uncertainties for MCFM NNLO calculation than the ResBos2 resummation calculation, which will propagate to the global fitting and lead to a worse description (larger χ^2) of data. For this reason, the final presentations of this work are mainly based on the ResBos2 resummation calculation.

We have identified the correlation between the experimental data points and the PDF flavors in a large momentum faction range $x \in [10^{-5}, 1]$, with the scale choice $Q = 100$ GeV, as an example. We find that the W^+ boson data can provide significant constraint on the $d(\bar{d})$ PDFs around $x \sim 10^{-3}$, while the W^- on the $u(\bar{u})$ PDFs. In comparison, the Z boson production can potentially constrain the $s(\bar{s})$ PDFs at $x \sim 10^{-2}$. With respect to the single differential distribution, the triple one in the ATLAS 8 TeV Z production can provide additional information. In addition, the LHCb measurements in the forward region can extend the sensitivity to the lower-x region.

With the ePump's PDF updating and the CT global fitting, we have examined the impact of the post-CT18 LHC Drell-Yan datasets, one at a time, on the CT18, CT18A, and CT18As PDFs. We remind the reader that the CT18A analysis includes the ATLAS 7 TeV W, Z precision data (ATL7WZ) [93] as an alternative fit due to its apparent tension with other preexisting data in the CT18, and the CT18As fit includes additional degrees of freedom in the strangeness PDF parametrization, which relaxes this tension. Overall, the impact of the post-CT18 LHC Drell-Yan data on the CT18 strangeness PDF is consistent with ATL7WZ in the CT18A fit. However, when examining more closely the $\bar{d}(d)$ PDFs, we obtain an opposite pull, driven by the ATL8W data, suggesting the tension with the ATL7WZ data. A similar tension from the LHCb8W data is observed at large x around $x \sim 0.3$, but with a minor impact due to the large PDF uncertainty in the large x region. With the additional shape parameter in the $s(\bar{s})$ PDFs of the CT18As fit, the tension between the ATL8W and ATL7WZ is relaxed.

We have also performed global fits to simultaneously include all these post-CT18 LHC Drell-Yan datasets, based on the CT18, CT18A and CT18As setups. The general feature agrees with the individual fits, i.e., the post-CT18 LHC Drell-Yan datasets pull the $s(\bar{s})$ PDFs in the same direction as CT18A fit, but with a weaker strength. In contrast, the post-CT18 LHC Drell-Yan datasets pull the $\bar{d}(d)$ PDFs to the opposite direction of the ATL7WZ data. The simultaneous inclusion of the ATL7WZ and post-CT18 LHC Drell-Yan datasets in the CT18A + nDY fit accumulates the pull on $s(\bar{s})$ PDFs, but balances the impact on $\bar{d}(d)$ PDFs. With the additional degrees of freedom in the CT18As fit, the impact of the post-CT18 LHC Drell-Yan data on the $s(\bar{s})$ PDFs is quite minimal, while the impact on $\bar{d}(d)$ PDFs remains. Regarding the PDF uncertainties, the post-CT18 LHC Drell-Yan data can significantly reduce the $s(\bar{s})$ PDF error bands, similar to the ATL7WZ data. The more flexible parametrization of the $s(\bar{s})$ PDFs in CT18As can enlarge the $\bar{d}(d)$ and $s(\bar{s})$ PDF error bands. Under such a condition, the post-CT18 LHC Drell-Yan data can help shrink the $d(\bar{d})$ PDF uncertainties but leave the $s(\bar{s})$ almost unchanged. With the inclusion of the lattice s_- data [111] in CT18As + Lat, the result of global fit CT18As + Lat + nDY is similar to CT18As + nDY, except the strangeness asymmetry s_- in the large-x region.

Finally, we have examined the impact of post-CT18 LHC Drell-Yan data on the parton luminosities as well as the corresponding phenomenological implications, by considering the correlation among W^+, W^-, Z, H, $t\bar{t}$, and $t\bar{t}H$ at the 14 TeV LHC, as examples. We find that the post-CT18 LHC Drell-Yan data normally enhance (reduce) the quark-related parton luminosities (such as $\mathcal{L}_{g\Sigma,q\bar{q},\Sigma\Sigma}$) at low (high)-invariant mass region. In comparison, the gg luminosity $\mathcal{L}_{gg}$ is reduced. Normally, the luminosity uncertainties shrink due to the constraining power of the post-CT18 LHC Drell-Yan datasets. The specific size of reduction can depend on the nonpertubative parametrization forms of PDFs. As a consequence of the quark-antiquark luminosity, the predicted cross sections for $W^\pm$ and Z productions at the 14 TeV LHC are enhanced, while their corresponding error bands are reduced. On the other hand, the total cross sections of Higgs, top-quark pair, and associated $t\bar{t}H$ processes are pulled to the smaller values, as a result of the reduction of gg luminosity.

As emphasized in the CT18 global analysis [14] as well as some follow-up studies [121], the inclusion of more high-precision data from the LHC does not necessarily yield the more precise PDFs, due to the pulls in different direction originated from tensions among the datasets. For this reason, we have released another fit such as CT18A PDFs to incorporate the additional ATLAS 7 TeV W, Z-precision data (ATL7WZ), which is found in tension with some existing datasets, such as the HERA I + II combined DIS data and the neutrino DIS dimuon production. In this study, we found that some of the post-CT18 LHC Drell-Yan data are consistent with the ATL7WZ data, such as ATL8Z3D and CMS13Z. But some tension with the

ATL7WZ data is still found among other datasets, such as the ATL8W data and, to a lesser extent, LHCb8W. With a more flexible nonperturbative parametrization of PDFs, this tension can be relaxed to some extent but not completely resolved. A full understanding of this tension is beyond the scope of this work, which is left for future work, especially the next round of CTEQ-TEA global analysis, to which this study will provide essential inputs.

ACKNOWLEDGMENTS

We would like to thank Yao Fu as well as other CTEQ-TEA colleagues for many helpful discussions. The work of A. Ablat, S. Dulat and I. Sitiwaldi are supported by the National Natural Science Foundation of China under Grant No. 11965020 and Grant No. 11847160, respectively. The work of K. X. is supported by the U.S. Department of Energy under Grant No. DE-SC0007914, the U.S. National Science Foundation under Grants No. PHY-1820760, and also in part by the PITT PACC. The work of C.-P. Yuan is supported by the U.S. National Science Foundation under Grant No. PHY-2013791. C.-P. Yuan is also grateful for the support from the Wu-Ki Tung endowed chair in particle physics.

APPENDIX: SUPPLEMENTARY FIGURES

The supplementary figures in this appendix have corresponding detailed explanations which are found in the main text.

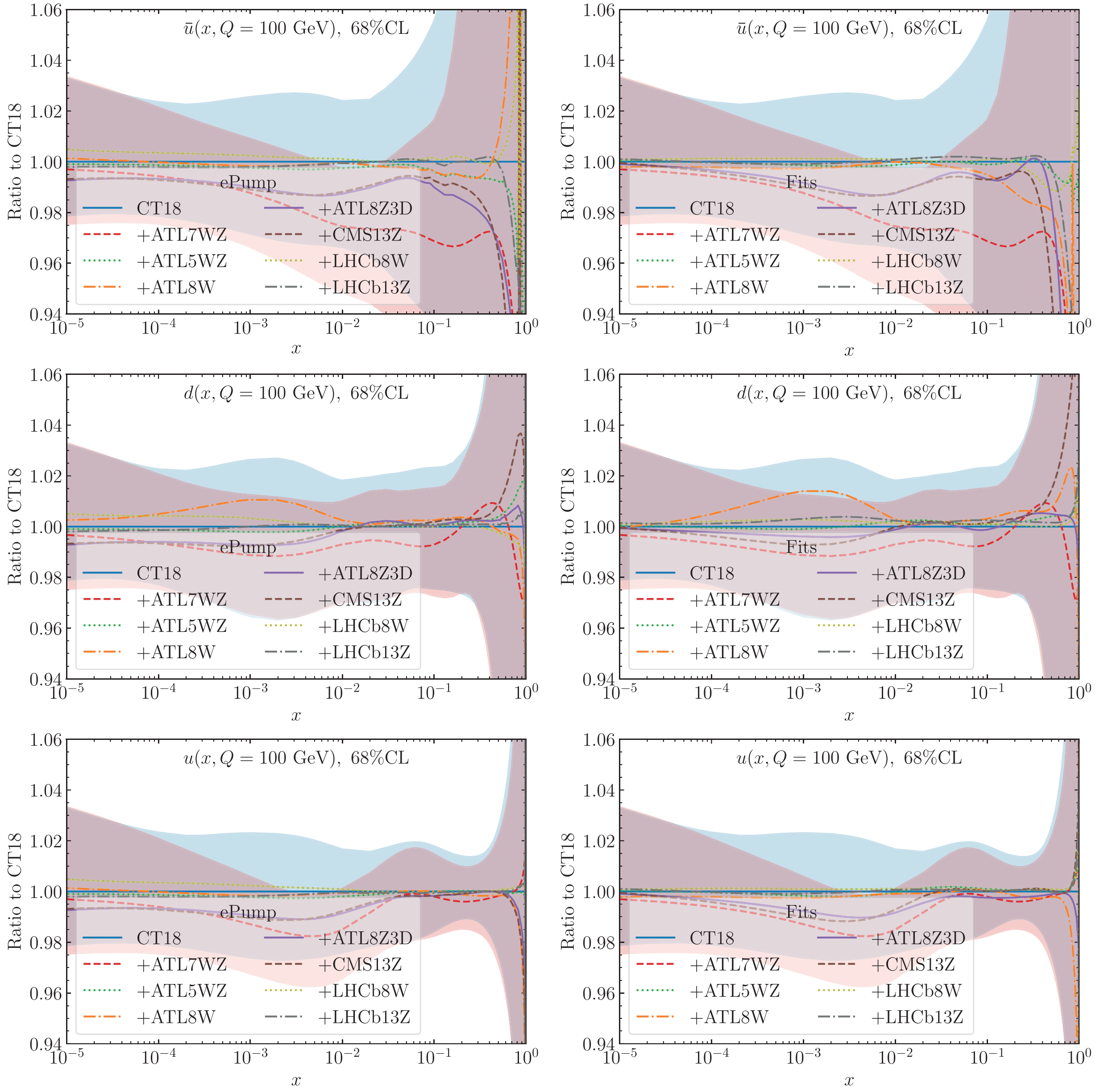

FIG. 15. Similar to Fig. 7, but for $\bar{u}, g, d, u$ PDFs at $Q = 100$ GeV.

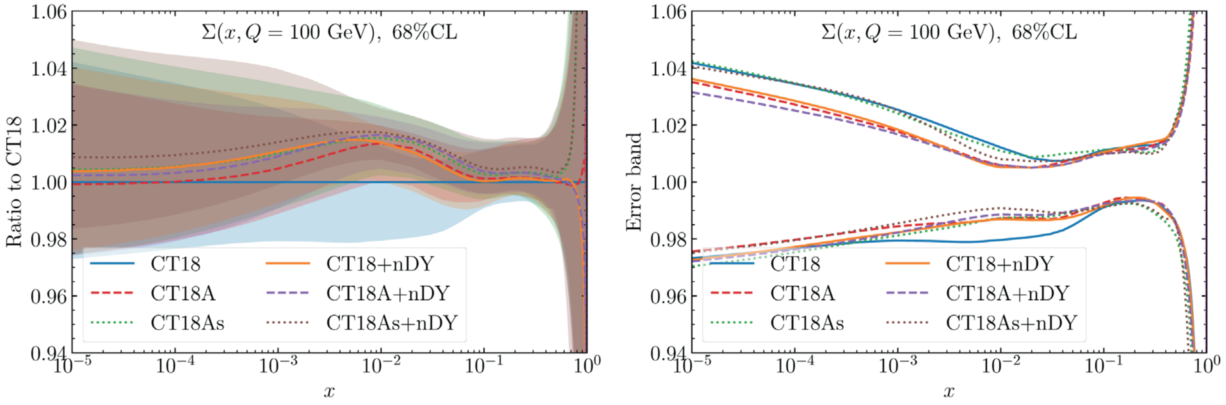

FIG. 16. Similar to Fig. 8, but for the flavor singlet Σ.

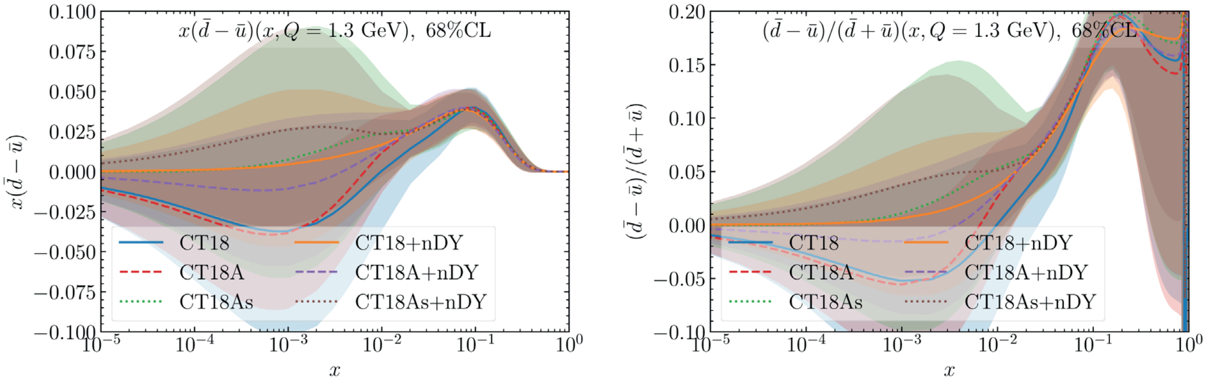

FIG. 17. Similar to Fig. 10, but for the $x(\bar{d}-\bar{u})$ and $(\bar{d}-\bar{u})/(\bar{d}+\bar{u})$ at $Q = 1.3$ GeV.

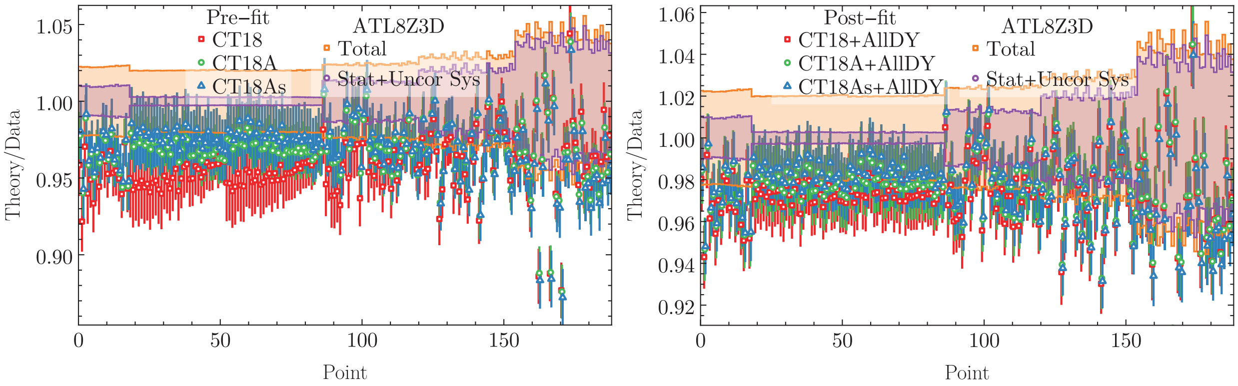

FIG. 18. Similar to Fig. 12, but for the ATLAS 8 TeV triple differential distributions.

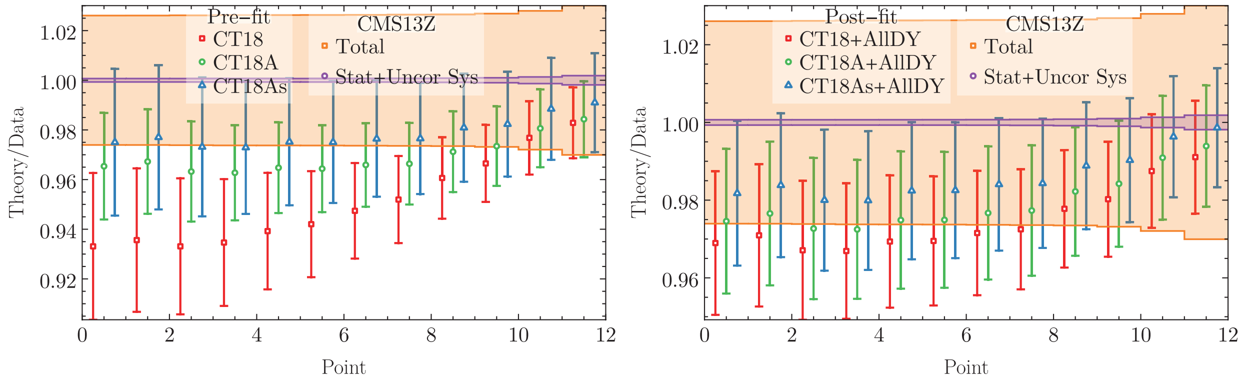

FIG. 19. Similar to Fig. 12, but for CMS 13 TeV Z production.

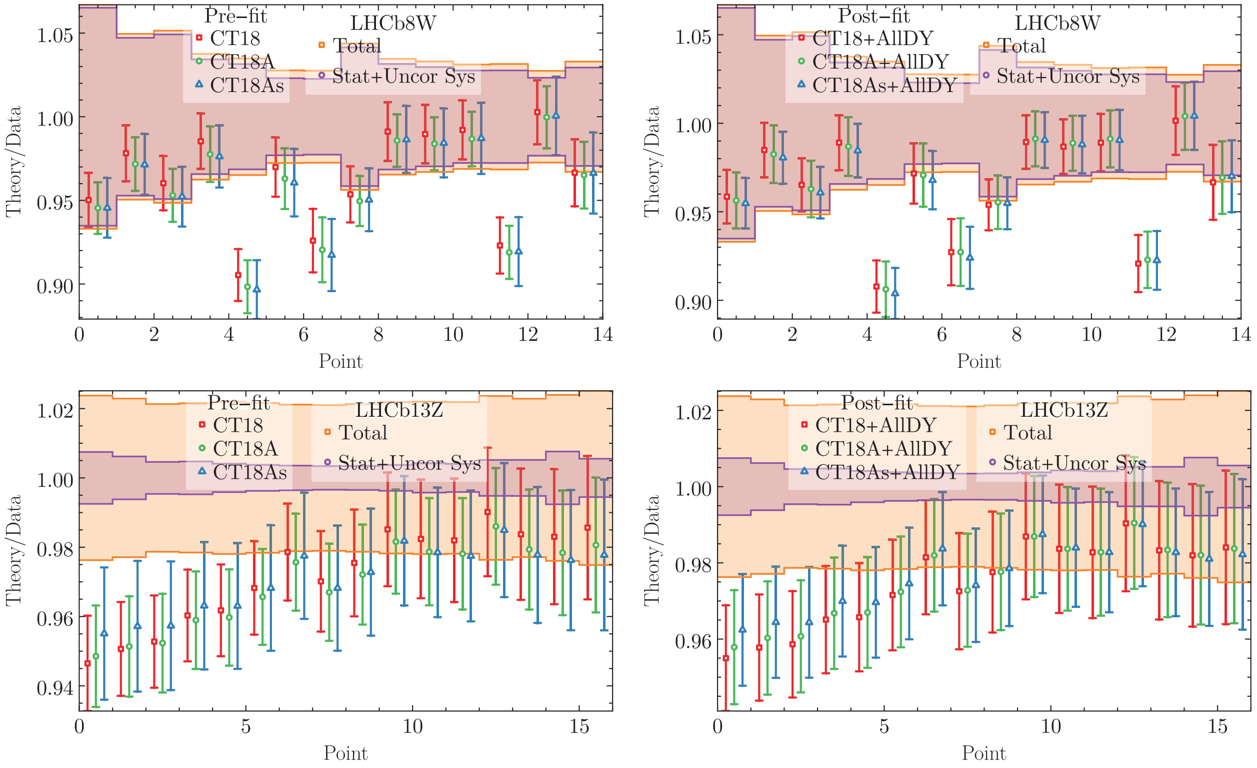

FIG. 20. Similar to Fig. 12, but for the LHCb 8 TeV W and 13 TeV Z datasets.

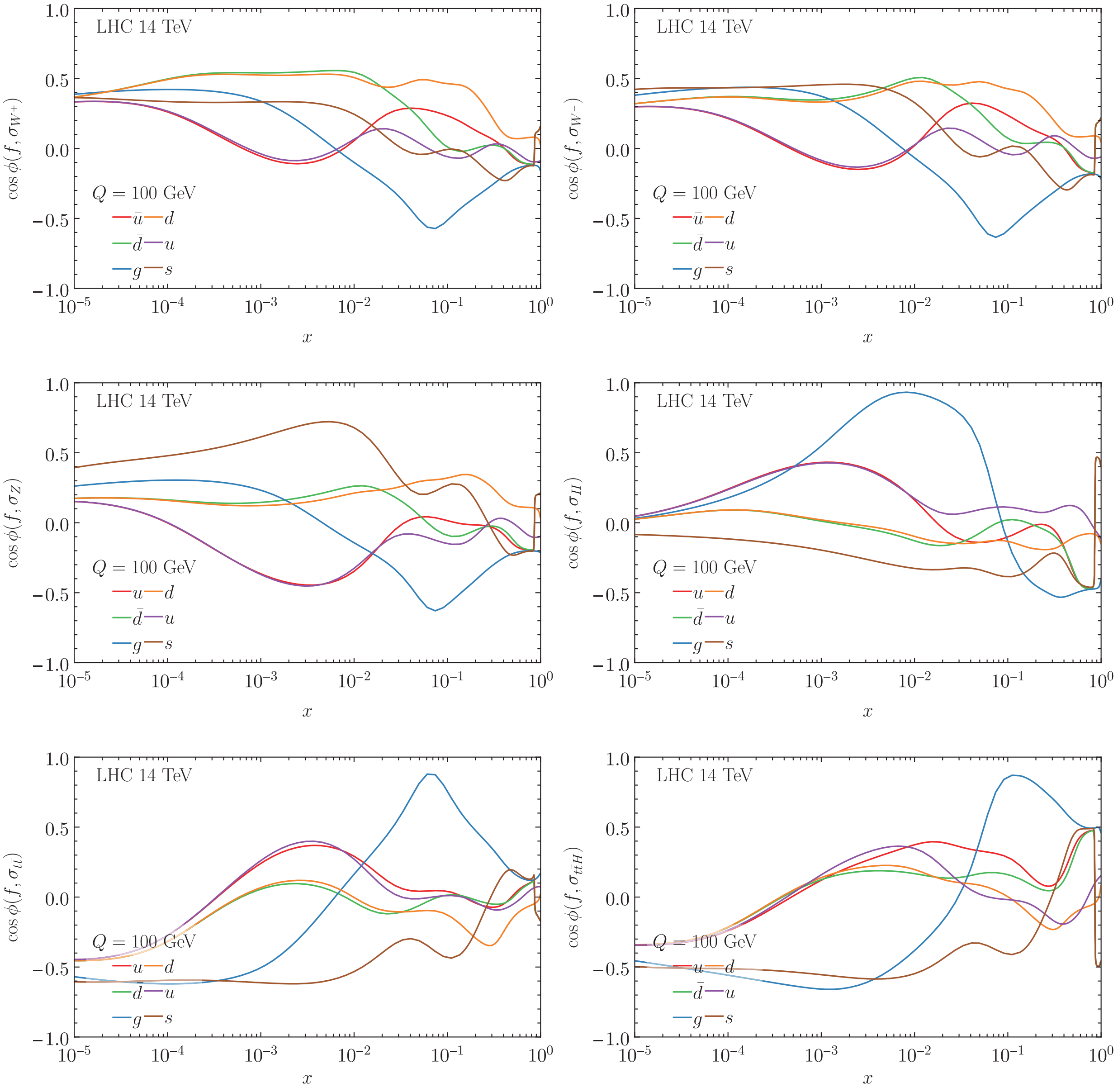

FIG. 21. The correlation cosine between the fiducial $W^{\pm}, Z$ and inclusive $t\bar{t}, H, t\bar{t}H$ cross sections with the CT18 PDF flavors at $Q = 100$ GeV.

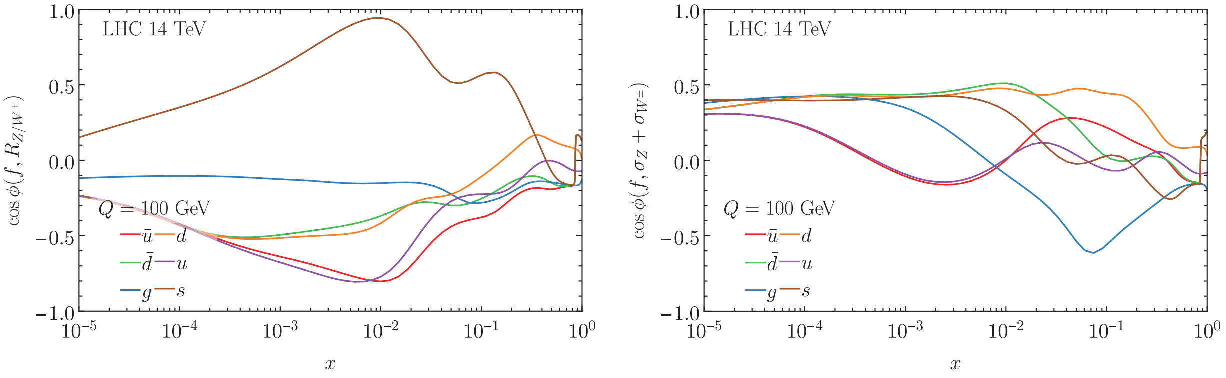

FIG. 22. The correlation cosine of the cross section ratio $R_{Z/W^{\pm}}$ and sum $\sigma_Z + \sigma_{W^{\pm}}$ with the CT18 PDF flavors at $Q = 100$ GeV.

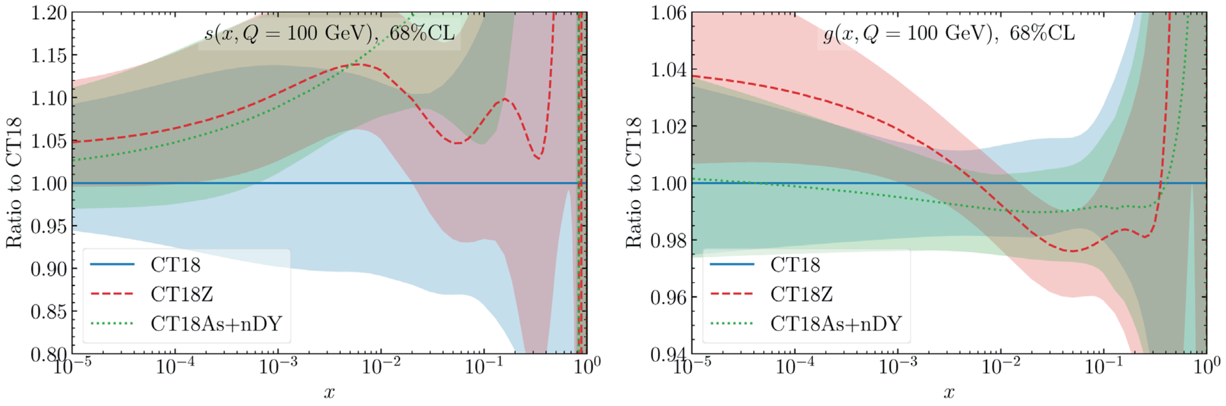

FIG. 23. The comparison of strangeness and gluon PDFs in the CT18, CT18Z, and CT18As + nDY fits at $Q = 100$ GeV.

---

[1] S. D. Drell and T.-M. Yan, Massive Lepton Pair Production in Hadron-Hadron Collisions at High-Energies, Phys. Rev. Lett. **25**, 316 (1970); **25**, 902(E) (1970).

[2] G. Arnison *et al.* (UA1 Collaboration), Experimental observation of isolated large transverse energy electrons with associated missing energy at $\sqrt{s} = 540$ GeV, Phys. Lett. **122B**, 103 (1983).

[3] M. Banner *et al.* (UA2 Collaboration), Observation of single isolated electrons of high transverse momentum in events with missing transverse energy at the CERN anti-p p collider, Phys. Lett. **122B**, 476 (1983).

[4] G. Arnison *et al.* (UA1 Collaboration), Experimental observation of lepton pairs of invariant mass around 95-GeV$/c^2$ at the CERN SPS collider, Phys. Lett. **126B**, 398 (1983).

[5] P. Bagnaia *et al.* (UA2 Collaboration), Evidence for $Z^0 \to e^+e^-$ at the CERN $\bar{p}p$ Collider, Phys. Lett. **129B**, 130 (1983).

[6] S. Chatrchyan *et al.* (CMS Collaboration), Measurement of the weak mixing angle with the Drell-Yan process in proton-proton collisions at the LHC, Phys. Rev. D **84**, 112002 (2011).

[7] A. M. Sirunyan *et al.* (CMS Collaboration), Measurement of the weak mixing angle using the forward-backward asymmetry of Drell-Yan events in pp collisions at 8 TeV, Eur. Phys. J. C **78**, 701 (2018).

[8] ATLAS Collaboration, Measurement of the effective leptonic weak mixing angle using electron and muon pairs from Z-boson decay in the ATLAS experiment at $\sqrt{s} = 8$ TeV, Report No. ATLAS-CONF-2018-037.

[9] A. M. Sirunyan *et al.* (CMS Collaboration), Determination of the strong coupling constant $\alpha_S(m_Z)$ from measurements of inclusive $W^\pm$ and Z boson production cross sections in proton-proton collisions at $\sqrt{\mathrm{s}} = 7$ and 8 TeV, J. High Energy Phys. 06 (2020) 018.

[10] S. Camarda, J. Cuth, and M. Schott, Determination of the muonic branching ratio of the W boson and its total width via cross-section measurements at the Tevatron and LHC, Eur. Phys. J. C **76**, 613 (2016).

[11] T. Aaltonen *et al.* (CDF Collaboration), High-precision measurement of the W boson mass with the CDF II detector, Science **376**, 170 (2022).

[12] A. Accardi, L. T. Brady, W. Melnitchouk, J. F. Owens, and N. Sato, Constraints on large-x parton distributions from new weak boson production and deep-inelastic scattering data, Phys. Rev. D **93**, 114017 (2016).

[13] S. Alekhin, J. Blümlein, S. Moch, and R. Placakyte, Parton distribution functions, α_s, and heavy-quark masses for LHC run II, Phys. Rev. D **96**, 014011 (2017).

[14] T.-J. Hou *et al.*, New CTEQ global analysis of quantum chromodynamics with high-precision data from the LHC, Phys. Rev. D **103**, 014013 (2021).

[15] S. Bailey, T. Cridge, L. A. Harland-Lang, A. D. Martin, and R. S. Thorne, Parton distributions from LHC, HERA, Tevatron and fixed target data: MSHT20 PDFs, Eur. Phys. J. C **81**, 341 (2021).

[16] R. D. Ball *et al.* (NNPDF Collaboration), Parton distributions from high-precision collider data, Eur. Phys. J. C **77**, 663 (2017).

[17] R. D. Ball *et al.* (NNPDF Collaboration), The path to proton structure at 1% accuracy, Eur. Phys. J. C **82**, 428 (2022).

[18] G. Aad *et al.*, Determination of the parton distribution functions of the proton using diverse ATLAS data from pp collisions at $\sqrt{s} = 7$, 8 and 13 TeV, Eur. Phys. J. C **82**, 438 (2022).

[19] G. Heinrich, Collider physics at the precision frontier, Phys. Rep. **922**, 1 (2021).

[20] A. Huss, J. Huston, S. Jones, and M. Pellen, Les Houches 2021: Physics at TeV Colliders: Report on the standard model precision wishlist, J. Phys. G **50**, 043001 (2023).

[21] V. Bertone, S. Carrazza, N. P. Hartland, and J. Rojo (NNPDF Collaboration), Illuminating the photon content of the proton within a global PDF analysis, SciPost Phys. **5**, 008 (2018).

[22] K. Xie, T. J. Hobbs, T.-J. Hou, C. Schmidt, M. Yan, and C. P. Yuan (CTEQ-TEA Collaborations), Photon PDF within the CT18 global analysis, Phys. Rev. D **105**, 054006 (2022).

[23] T. Cridge, L. A. Harland-Lang, A. D. Martin, and R. S. Thorne, QED parton distribution functions in the MSHT20 fit, Eur. Phys. J. C **82**, 90 (2022).

[24] R. Hamberg, W. L. van Neerven, and T. Matsuura, A complete calculation of the order α_s^2 correction to the Drell-Yan K factor, Nucl. Phys. **B359**, 343 (1991); **B644**, 403 (2002).

[25] C. Anastasiou, L. J. Dixon, K. Melnikov, and F. Petriello, Dilepton Rapidity Distribution in the Drell-Yan Process at NNLO in QCD, Phys. Rev. Lett. **91**, 182002 (2003).

[26] C. Anastasiou, L. J. Dixon, K. Melnikov, and F. Petriello, High precision QCD at hadron colliders: Electroweak gauge boson rapidity distributions at NNLO, Phys. Rev. D **69**, 094008 (2004).

[27] K. Melnikov and F. Petriello, The W Boson Production Cross Section at the LHC through $O(\alpha_s^2)$, Phys. Rev. Lett. **96**, 231803 (2006).

[28] K. Melnikov and F. Petriello, Electroweak gauge boson production at hadron colliders through $O(\alpha_s^2)$, Phys. Rev. D **74**, 114017 (2006).

[29] S. Catani, L. Cieri, G. Ferrera, D. de Florian, and M. Grazzini, Vector Boson Production at Hadron Colliders: A Fully Exclusive QCD Calculation at NNLO, Phys. Rev. Lett. **103**, 082001 (2009).

[30] S. Catani and M. Grazzini, An NNLO Subtraction Formalism in Hadron Collisions and its Application to Higgs Boson Production at the LHC, Phys. Rev. Lett. **98**, 222002 (2007).

[31] M. Grazzini, S. Kallweit, and M. Wiesemann, Fully differential NNLO computations with MATRIX, Eur. Phys. J. C **78**, 537 (2018).

[32] Y. Li and F. Petriello, Combining QCD and electroweak corrections to dilepton production in FEWZ, Phys. Rev. D **86**, 094034 (2012).

[33] R. Gavin, Y. Li, F. Petriello, and S. Quackenbush, W Physics at the LHC with FEWZ 2.1, Comput. Phys. Commun. **184**, 208 (2013).

[34] R. Boughezal, J. M. Campbell, R. K. Ellis, C. Focke, W. Giele, X. Liu, F. Petriello, and C. Williams, Color singlet production at NNLO in MCFM, Eur. Phys. J. C **77**, 7 (2017).

[35] J. Campbell and T. Neumann, Precision phenomenology with MCFM, J. High Energy Phys. 12 (2019) 034.

[36] J. C. Collins, D. E. Soper, and G. F. Sterman, Transverse momentum distribution in Drell-Yan pair and W and Z boson production, Nucl. Phys. **B250**, 199 (1985).

[37] S. Catani, L. Cieri, D. de Florian, G. Ferrera, and M. Grazzini, Universality of transverse-momentum resummation and hard factors at the NNLO, Nucl. Phys. **B881**, 414 (2014).

[38] C. W. Bauer, S. Fleming, and M. E. Luke, Summing Sudakov logarithms in $B \to X_s\gamma$ in effective field theory, Phys. Rev. D **63**, 014006 (2000).

[39] C. W. Bauer, S. Fleming, D. Pirjol, and I. W. Stewart, An effective field theory for collinear and soft gluons: Heavy to light decays, Phys. Rev. D **63**, 114020 (2001).

[40] C. W. Bauer, D. Pirjol, and I. W. Stewart, Soft collinear factorization in effective field theory, Phys. Rev. D **65**, 054022 (2002).

[41] C. W. Bauer, S. Fleming, D. Pirjol, I. Z. Rothstein, and I. W. Stewart, Hard scattering factorization from effective field theory, Phys. Rev. D **66**, 014017 (2002).

[42] M. Beneke, A. P. Chapovsky, M. Diehl, and T. Feldmann, Soft collinear effective theory and heavy to light currents beyond leading power, Nucl. Phys. **B643**, 431 (2002).

[43] T. Becher and M. Neubert, Drell-Yan production at small q_T, transverse parton distributions and the collinear anomaly, Eur. Phys. J. C **71**, 1665 (2011).

[44] T. Becher, M. Neubert, and D. Wilhelm, Electroweak gauge-boson production at small q_T: Infrared safety from the collinear anomaly, J. High Energy Phys. 02 (2012) 124.

[45] T. Becher, M. Neubert, and D. Wilhelm, Higgs-boson production at small transverse momentum, J. High Energy Phys. 05 (2013) 110.

[46] G. A. Ladinsky and C. P. Yuan, The nonperturbative regime in QCD resummation for gauge boson production at hadron colliders, Phys. Rev. D **50**, R4239 (1994).

[47] C. Balazs and C. P. Yuan, Soft gluon effects on lepton pairs at hadron colliders, Phys. Rev. D **56**, 5558 (1997).

[48] J. P. Isaacson, ResBos2: Precision resummation for the LHC era, Ph.D. thesis, Michigan State University, 2017.

[49] S. Catani, D. de Florian, G. Ferrera, and M. Grazzini, Vector boson production at hadron colliders: Transverse-momentum resummation and leptonic decay, J. High Energy Phys. 12 (2015) 047.

[50] G. Bozzi, S. Catani, G. Ferrera, D. de Florian, and M. Grazzini, Transverse-momentum resummation: A perturbative study of Z production at the Tevatron, Nucl. Phys. **B815**, 174 (2009).

[51] G. Bozzi, S. Catani, G. Ferrera, D. de Florian, and M. Grazzini, Production of Drell-Yan lepton pairs in hadron collisions: Transverse-momentum resummation at next-to-next-to-leading logarithmic accuracy, Phys. Lett. B **696**, 207 (2011).

[52] S. Camarda *et al.*, DYTurbo: Fast predictions for Drell-Yan processes, Eur. Phys. J. C **80**, 251 (2020); **80**, 440(E) (2020).

[53] T. Becher and T. Neumann, Fiducial q_T resummation of color-singlet processes at $\mathrm{N}^3\mathrm{LL} + \mathrm{NNLO}$, J. High Energy Phys. 03 (2021) 199.

[54] C. Duhr, F. Dulat, and B. Mistlberger, Drell-Yan Cross Section to Third Order in the Strong Coupling Constant, Phys. Rev. Lett. **125**, 172001 (2020).

[55] C. Duhr and B. Mistlberger, Lepton-pair production at hadron colliders at N^3LO in QCD, J. High Energy Phys. 03 (2022) 116.

[56] X. Chen, T. Gehrmann, N. Glover, A. Huss, T.-Z. Yang, and H. X. Zhu, Dilepton Rapidity Distribution in Drell-Yan Production to Third Order in QCD, Phys. Rev. Lett. **128**, 052001 (2022).

[57] S. Camarda, L. Cieri, and G. Ferrera, Drell–Yan lepton-pair production: qT resummation at N3LL accuracy and fiducial cross sections at N3LO, Phys. Rev. D **104**, L111503 (2021).

[58] X. Chen, T. Gehrmann, E. W. N. Glover, A. Huss, P. F. Monni, E. Re, L. Rottoli, and P. Torrielli, Third-Order

Fiducial Predictions for Drell-Yan Production at the LHC, Phys. Rev. Lett. **128**, 252001 (2022).

[59] T. Neumann and J. Campbell, Fiducial Drell-Yan production at the LHC improved by transverse-momentum resummation at N4LLp + N3LO, Phys. Rev. D **107**, L011506 (2023).

[60] U. Baur, O. Brein, W. Hollik, C. Schappacher, and D. Wackeroth, Electroweak radiative corrections to neutral current Drell-Yan processes at hadron colliders, Phys. Rev. D **65**, 033007 (2002).

[61] G. Balossini, G. Montagna, C. M. Carloni Calame, M. Moretti, M. Treccani, O. Nicrosini, F. Piccinini, and A. Vicini, Electroweak & QCD corrections to Drell Yan processes, Acta Phys. Polon. B **39**, 1675 (2008).

[62] R. Bonciani, L. Buonocore, M. Grazzini, S. Kallweit, N. Rana, F. Tramontano, and A. Vicini, Mixed Strong-Electroweak Corrections to the Drell-Yan Process, Phys. Rev. Lett. **128**, 012002 (2022).

[63] S. Dulat, T.-J. Hou, J. Gao, M. Guzzi, J. Huston, P. Nadolsky, J. Pumplin, C. Schmidt, D. Stump, and C. P. Yuan, New parton distribution functions from a global analysis of quantum chromodynamics, Phys. Rev. D **93**, 033006 (2016).

[64] S. Alekhin, A. Kardos, S. Moch, and Z. Trócsányi, Precision studies for Drell–Yan processes at NNLO, Eur. Phys. J. C **81**, 573 (2021).

[65] N. Zakharchuk, Measurement of Z-boson production cross sections at $\sqrt{s} = 13$ TeV and $t\bar{t}$ to Z-boson cross-section ratios with the ATLAS detector at the LHC, Ph.D. thesis, Hamburg University, Hamburg, 2018.

[66] T.-J. Hou, H.-W. Lin, M. Yan, and C. P. Yuan, Impact of lattice strangeness asymmetry data in the CTEQ-TEA global analysis, Phys. Rev. D **107**, 076018 (2023).

[67] C. Schmidt, J. Pumplin, C. P. Yuan, and P. Yuan, Updating and optimizing error parton distribution function sets in the Hessian approach, Phys. Rev. D **98**, 094005 (2018).

[68] T.-J. Hou, Z. Yu, S. Dulat, C. Schmidt, and C. P. Yuan, Updating and optimizing error parton distribution function sets in the Hessian approach. II, Phys. Rev. D **100**, 114024 (2019).

[69] R. Aaij *et al.* (LHCb Collaboration), Inclusive W and Z production in the forward region at $\sqrt{s} = 7$ TeV, J. High Energy Phys. 06 (2012) 058.

[70] S. Chatrchyan *et al.* (CMS Collaboration), Measurement of the muon charge asymmetry in inclusive $pp \to W + X$ production at $\sqrt{s} = 7$ TeV and an improved determination of light parton distribution functions, Phys. Rev. D **90**, 032004 (2014).

[71] S. Chatrchyan *et al.* (CMS Collaboration), Measurement of the Electron Charge Asymmetry in Inclusive W Production in pp Collisions at $\sqrt{s} = 7$ TeV, Phys. Rev. Lett. **109**, 111806 (2012).

[72] G. Aad *et al.* (ATLAS Collaboration), Measurement of the inclusive $W^{\pm}$ and Z/gamma cross sections in the electron and muon decay channels in pp collisions at $\sqrt{s} = 7$ TeV with the ATLAS detector, Phys. Rev. D **85**, 072004 (2012).

[73] R. Aaij *et al.* (LHCb Collaboration), Measurement of the forward Z boson production cross-section in pp collisions at $\sqrt{s} = 7$ TeV, J. High Energy Phys. 08 (2015) 039.

[74] T. Carli, D. Clements, A. Cooper-Sarkar, C. Gwenlan, G. P. Salam, F. Siegert, P. Starovoitov, and M. Sutton, *A posteriori* inclusion of parton density functions in NLO QCD final-state calculations at hadron colliders: The APPLGRID Project, Eur. Phys. J. C **66**, 503 (2010).

[75] J. M. Campbell and R. K. Ellis, MCFM for the Tevatron and the LHC, Nucl. Phys. **B205–206**, 10 (2010).

[76] V. Bertone, R. Frederix, S. Frixione, J. Rojo, and M. Sutton, aMCfast: Automation of fast NLO computations for PDF fits, J. High Energy Phys. 08 (2014) 166.

[77] J. M. Campbell, R. K. Ellis, and W. T. Giele, A multi-threaded version of MCFM, Eur. Phys. J. C **75**, 246 (2015).

[78] M. Aaboud *et al.* (ATLAS Collaboration), Measurements of W and Z boson production in pp collisions at $\sqrt{s} = 5.02$ TeV with the ATLAS detector, Eur. Phys. J. C **79**, 128 (2019); **79**, 374(E) (2019).

[79] J. Gao and P. Nadolsky, A meta-analysis of parton distribution functions, J. High Energy Phys. 07 (2014) 035.

[80] G. Aad *et al.* (ATLAS Collaboration), Measurement of the cross-section and charge asymmetry of W bosons produced in proton–proton collisions at $\sqrt{s} = 8$ TeV with the ATLAS detector, Eur. Phys. J. C **79**, 760 (2019).

[81] M. Aaboud *et al.* (ATLAS Collaboration), Measurement of the Drell-Yan triple-differential cross section in pp collisions at $\sqrt{s} = 8$ TeV, J. High Energy Phys. 12 (2017) 059.

[82] J. C. Collins and D. E. Soper, Angular distribution of dileptons in high-energy hadron collisions, Phys. Rev. D **16**, 2219 (1977).

[83] S. Alekhin *et al.*, HERAFitter, Eur. Phys. J. C **75**, 304 (2015).

[84] J. Currie, E. W. N. Glover, and J. Pires, Next-to-Next-to Leading Order QCD Predictions for Single Jet Inclusive Production at the LHC, Phys. Rev. Lett. **118**, 072002 (2017).

[85] A. M. Sirunyan *et al.* (CMS Collaboration), Measurements of differential Z boson production cross sections in proton-proton collisions at $\sqrt{s} = 13$ TeV, J. High Energy Phys. 12 (2019) 061.

[86] A. Banfi, S. Redford, M. Vesterinen, P. Waller, and T. R. Wyatt, Optimisation of variables for studying dilepton transverse momentum distributions at hadron colliders, Eur. Phys. J. C **71**, 1600 (2011).

[87] A. Banfi, M. Dasgupta, S. Marzani, and L. Tomlinson, Predictions for Drell-Yan ϕ^* and Q_T observables at the LHC, Phys. Lett. B **715**, 152 (2012).

[88] R. Aaij *et al.* (LHCb Collaboration), Measurement of forward $W \to e\nu$ production in pp collisions at $\sqrt{s} = 8$ TeV, J. High Energy Phys. 10 (2016) 030.

[89] R. Aaij *et al.* (LHCb Collaboration), Measurement of the forward Z boson production cross-section in pp collisions at $\sqrt{s} = 13$ TeV, J. High Energy Phys. 09 (2016) 136.

[90] R. Aaij *et al.* (LHCb Collaboration), Precision measurement of forward Z boson production in proton-proton collisions at $\sqrt{s} = 13$ TeV, J. High Energy Phys. 07 (2022) 026.

[91] G. Aad *et al.* (ATLAS Collaboration), Measurement of the low-mass Drell-Yan differential cross section at $\sqrt{s} = 7$ TeV using the ATLAS detector, J. High Energy Phys. 06 (2014) 112.

[92] G. Aad *et al.* (ATLAS Collaboration), Measurement of the high-mass Drell–Yan differential cross-section in pp collisions at sqrt(s)=7 TeV with the ATLAS detector, Phys. Lett. B **725**, 223 (2013).

[93] M. Aaboud *et al.* (ATLAS Collaboration), Precision measurement and interpretation of inclusive W^+, W^- and Z/γ^* production cross sections with the ATLAS detector, Eur. Phys. J. C **77**, 367 (2017).

[94] G. Aad *et al.* (ATLAS Collaboration), Measurement of the Z/γ^* boson transverse momentum distribution in pp collisions at $\sqrt{s}=7$ TeV with the ATLAS detector, J. High Energy Phys. 09 (2014) 145.

[95] G. Aad *et al.* (ATLAS Collaboration), Measurement of the double-differential high-mass Drell-Yan cross section in pp collisions at $\sqrt{s}=8$ TeV with the ATLAS detector, J. High Energy Phys. 08 (2016) 009.

[96] G. Aad *et al.* (ATLAS Collaboration), Measurement of the transverse momentum and ϕ^*_η distributions of Drell–Yan lepton pairs in proton–proton collisions at $\sqrt{s}=8$ TeV with the ATLAS detector, Eur. Phys. J. C **76**, 291 (2016).

[97] G. Aad *et al.* (ATLAS Collaboration), Measurement of $W^\pm$ and Z-boson production cross sections in pp collisions at $\sqrt{s}=13$ TeV with the ATLAS detector, Phys. Lett. B **759**, 601 (2016).

[98] G. Aad *et al.* (ATLAS Collaboration), Measurement of $W^\pm$-boson and Z-boson production cross-sections in pp collisions at $\sqrt{s}=2.76$ TeV with the ATLAS detector, Eur. Phys. J. C **79**, 901 (2019).

[99] G. Aad *et al.* (ATLAS Collaboration), Measurement of the transverse momentum distribution of Drell–Yan lepton pairs in proton–proton collisions at $\sqrt{s}=13$ TeV with the ATLAS detector, Eur. Phys. J. C **80**, 616 (2020).

[100] S. Chatrchyan *et al.* (CMS Collaboration), Measurement of the lepton charge asymmetry in inclusive W production in pp collisions at $\sqrt{s}=7$ TeV, J. High Energy Phys. 04 (2011) 050.

[101] S. Chatrchyan *et al.* (CMS Collaboration), Measurement of the rapidity and transverse momentum distributions of Z bosons in pp collisions at $\sqrt{s}=7$ TeV, Phys. Rev. D **85**, 032002 (2012).

[102] V. Khachatryan *et al.* (CMS Collaboration), Measurement of the differential cross section and charge asymmetry for inclusive $\mathrm{pp}\to\mathrm{W}^\pm+X$ production at $\sqrt{s}=8$ TeV, Eur. Phys. J. C **76**, 469 (2016).

[103] S. Chatrchyan *et al.* (CMS Collaboration), Measurement of the differential and double-differential Drell-Yan cross sections in proton-proton collisions at $\sqrt{s}=7$ TeV, J. High Energy Phys. 12 (2013) 030.

[104] V. Khachatryan *et al.* (CMS Collaboration), Measurement of the Z boson differential cross section in transverse momentum and rapidity in proton–proton collisions at 8 TeV, Phys. Lett. B **749**, 187 (2015).

[105] A. M. Sirunyan *et al.* (CMS Collaboration), Measurement of differential cross sections in the kinematic angular variable ϕ^* for inclusive Z boson production in pp collisions at $\sqrt{s}=8$ TeV, J. High Energy Phys. 03 (2018) 172.

[106] A. M. Sirunyan *et al.* (CMS Collaboration), Measurements of the W boson rapidity, helicity, double-differential cross sections, and charge asymmetry in pp collisions at $\sqrt{s}=13$ TeV, Phys. Rev. D **102**, 092012 (2020).

[107] A. M. Sirunyan *et al.* (CMS Collaboration), Measurement of the differential Drell-Yan cross section in proton-proton collisions at $\sqrt{s}=13$ TeV, J. High Energy Phys. 12 (2019) 059.

[108] R. Aaij *et al.* (LHCb Collaboration), Measurement of the cross-section for $Z\to e^+e^-$ production in pp collisions at $\sqrt{s}=7$ TeV, J. High Energy Phys. 02 (2013) 106.

[109] R. Aaij *et al.* (LHCb Collaboration), Measurement of forward W and Z boson production in pp collisions at $\sqrt{s}=8$ TeV, J. High Energy Phys. 01 (2016) 155.

[110] R. Aaij *et al.* (LHCb Collaboration), Measurement of forward $\mathrm{Z}\to\mathrm{e}^+\mathrm{e}^-$ production at $\sqrt{s}=8$ TeV, J. High Energy Phys. 05 (2015) 109.

[111] R. Zhang, H.-W. Lin, and B. Yoon, Probing nucleon strange and charm distributions with lattice QCD, Phys. Rev. D **104**, 094511 (2021).

[112] J. M. Campbell, J. W. Huston, and W. J. Stirling, Hard interactions of quarks and gluons: A primer for LHC physics, Rep. Prog. Phys. **70**, 89 (2007).

[113] M. Czakon and A. Mitov, Top++: A program for the calculation of the top-pair cross-section at hadron colliders, Comput. Phys. Commun. **185**, 2930 (2014).

[114] M. Bonvini, S. Marzani, C. Muselli, and L. Rottoli, On the Higgs cross section at $\mathrm{N^3LO}+\mathrm{N^3LL}$ and its uncertainty, J. High Energy Phys. 08 (2016) 105.

[115] R. Frederix, S. Frixione, V. Hirschi, D. Pagani, H. S. Shao, and M. Zaro, The automation of next-to-leading order electroweak calculations, J. High Energy Phys. 07 (2018) 185; 11 (2021) 085(E).

[116] S. Carrazza, E. R. Nocera, C. Schwan, and M. Zaro, PineAPPL: Combining EW and QCD corrections for fast evaluation of LHC processes, J. High Energy Phys. 12 (2020) 108.

[117] P. M. Nadolsky, H.-L. Lai, Q.-H. Cao, J. Huston, J. Pumplin, D. Stump, W.-K. Tung, and C. P. Yuan, Implications of CTEQ global analysis for collider observables, Phys. Rev. D **78**, 013004 (2008).

[118] F. Landry, R. Brock, P. M. Nadolsky, and C. P. Yuan, Tevatron Run-1Z boson data and Collins-Soper-Sterman resummation formalism, Phys. Rev. D **67**, 073016 (2003).

[119] F. Landry, R. Brock, G. Ladinsky, and C. P. Yuan, New fits for the nonperturbative parameters in the CSS resummation formalism, Phys. Rev. D **63**, 013004 (2001).

[120] P. Sun, J. Isaacson, C. P. Yuan, and F. Yuan, Nonperturbative functions for SIDIS and Drell–Yan processes, Int. J. Mod. Phys. A **33**, 1841006 (2018).

[121] A. Courtoy, J. Huston, P. Nadolsky, K. Xie, M. Yan, and C. P. Yuan, Parton distributions need representative sampling, Phys. Rev. D **107**, 034008 (2023).